

Planar Bipedal Jumping Gaits With Stable Landing

Dip Goswami, *Student Member, IEEE*, and Prahlad Vadakkepat, *Senior Member, IEEE*

Abstract—In this paper, landing stability of jumping gaits is studied for a four-link planar biped model. Rotation of the foot during the landing phase leads to underactuation due to the passive degree of freedom at the toe, which results in nontrivial zero dynamics (ZD). Compliance between the foot and ground is modeled as a spring–damper system. Rotation of the foot along with the compliance model introduces switching in the ZD. The stability conditions for the “switching ZD” and closed-loop dynamics (CLD) are established. “Critical potential index” and “critical kinetic index” are introduced as measures of the stability of the CLD of the biped during landing. Landing stability is achieved by utilizing the stability conditions. Stable jumping motion is experimentally realized on a biped robot.

Index Terms—Biped robot, closed-loop dynamics (CLD), critical potential index and critical kinetic index, jumping gaits, landing stability, multiple Lyapunov function (MLF), singular perturbation, switching zero dynamics (ZD).

I. INTRODUCTION

ZERO moment point (ZMP) is a widely used concept to analyze postural stability of legged systems [1]. The ZMP is the point on the ground where the resultant of moments acting on the legged system is zero. To maintain postural stability in legged systems, the ZMP is kept within the area covered by the foot, i.e., the support polygon [2]–[4]. Biped locomotion is normally considered with flat foot while utilizing the ZMP-based stability criterion [3], [4]. Unbalanced moment on the foot leads to foot rotation about a point on the foot boundary. Rotation of the foot is an important aspect to look into while addressing stable locomotion. The foot rotation indicator (FRI) point explains the occurrence of foot rotation [5]. If the FRI point is outside the footprint area, the foot rotates about a certain point on the foot boundary. The foot rotation changes the absolute orientation of the biped bringing in a passive degree of freedom (DOF) that makes the bipedal systems *underactuated*.

The absolute orientation of the biped is considered as an additional passive DOF in certain biped models [6]–[9]. Such biped models are underactuated in nature resulting in nontrivial zero dynamics (ZD) [10]. It is essential to investigate the stability of the associated ZD while dealing with underactuated systems. Periodic trajectories with the specific properties result in stable ZD of a two-link acrobat [9]. The periodic nature of the locomotion/gait is utilized to stabilize the ZD [6], [7], [11], [12]. A Poincaré return map is an effective tool to validate periodicity and *orbital stability* [6], [7]. Simplified biped models such as

spring–damper systems are helpful in establishing periodicity in locomotion [11].

As ZMP criterion is not applicable to point foot bipeds, the concept of orbital stability is useful while dealing with the associated stability issues [6], [7], [12]. By periodically attaining certain postures, even though statically unstable, the orbital stability is achieved. Similar concepts are useful in analyzing stability of periodic activities such as running and hopping.

Fast dynamical activities like running, jumping, or hopping are reported [2], [11]–[13] and experimentally realized [14], [15]. The flight phase is common in these activities when the physical system loses contact with the ground. In the flight phase, it is noticeable that ground reaction force (GRF) becomes zero, and angular momentum is conserved.

GRF is often used as a feedback to control the jumping motion [16]–[19]. GRF data obtained from human jumping phases are utilized to compute the biped jumping gaits by optimizing the inertial forces [16]. Simplification of bipedal dynamics, for example, the inverted pendulum model, is helpful in developing force-control strategies for jumping gait generation [17], [18]. Time of application of the control scheme is important in designing the effective force-control strategies for vertical jumping [19].

In a number of studies, angular momentum is used for jumping motion control [20], [21], [23]. Mita *et al.* utilize an angular momentum conservation principle to develop an optimal control strategy to produce jumping motion [20]. The flight phase is initiated by nonzero angular momentum of a two-link planar robot in [20]. The motion of a four-link gymnastic robot is controlled using feedback linearization by Sobotka and Buss [21]. *Non-holonomic* motion planning needs identification of few discrete states during flight phase [21]. Hyon *et al.* [23] report backhandspring experiment by controlling the angular momentum about center of mass (CM).

Unlike running and hopping, jumping is aperiodic. Hence, the concepts of periodicity and orbital stability are not applicable to resolve the stability issues involved in jumping gaits. Although static stability is possible in point foot bipeds, the presence of the foot essentially provides greater stability margin. Two important issues arise while considering the landing stability of jumping gaits for the bipeds with nontrivial foot size. The first issue is related to the modeling of the contact surface between the foot and the ground, i.e., foot compliance [6], [22]. Foot compliance is required to model the contact surface between the foot and the ground surface while modeling biped dynamics in the presence of the foot. The traditional concepts such as ZMP and FRI are not suitable to address the stability when foot compliance model is included in the system (or biped’s) dynamics. Second issue is related to the stability in the presence of the foot rotation in biped locomotion. In flat-foot postures, ZMP and FRI use the torque generated at the toe–ground contact point due to GRF.

Manuscript received December 24, 2008; revised April 2, 2009. First published July 24, 2009; current version published October 9, 2009. This paper was recommended for publication by Associate Editor K. Yamane and Editor W. K. Chung upon evaluation of the reviewers’ comments.

The authors are with the Department of Electrical and Computer Engineering, National University of Singapore, Singapore 117576 (e-mail: dip.goswami@ieee.org; prahlad@ieee.org).

Color versions of one or more of the figures in this paper are available online at <http://ieeexplore.ieee.org>.

Digital Object Identifier 10.1109/TRO.2009.2026502

Such torques due to GRF become zero when the foot is rotated because GRF acts at the point of foot rotation. Therefore, ZMP and FRI are not suitable for postural stability analysis when the foot is already rotated. Stability considerations with foot rotation for the activities like back-handspring, handstand, and somersault are reported in [23] and [24], which are confined to gait generation and control strategies. In the landing phase of jumping gaits, the biped postures may be either with foot rotation or with the foot being flat on the ground (modeled by foot compliance). The presence of flat-foot postures and rotated foot scenarios necessitates further stability analysis with the foot compliance model being included in the biped dynamics.

Stability analysis associated with the foot compliance model in the presence of foot rotation during the landing phase of jumping gaits is the major motivation of this paper. The jumping gait is generated for a biped with the foot compliance model as a spring–damper system [22]. The control is formulated as an *output zeroing* problem [10] where the *output functions* are constructed according to the desired jumping performance. During the landing phase (with foot rotation), the biped model becomes underactuated due to the presence of passive DOF at the contact between the toe and the ground. The underactuation results in 2-D ZD. The biped switches between the configuration with foot rotation to the one with flat foot or *vice versa* during the landing phase. The associated ZD is named as “*switching ZD (SZD)*.” The conditions for landing stability are derived to stabilize the switching system. The stability of the closed-loop system further depends on the two quantities that are named “*critical potential index*” and “*critical kinetic index*.” The jumping motion is experimentally realized and stability conditions are validated.

Section II describes the biped jumping robot and the computation of the associated dynamics. The control strategy is discussed in Section III, while a selection procedure of desired gaits for the *output functions* is discussed in Section IV. The landing stability analysis is provided in Section V. The simulations and experimentations of the jumping gait are described in Section VI, and conclusions are drawn in Section VII.

II. BIPED JUMPER

A. Biped Jumper: BRAIL 2.0

Bio-Robotics Activities in Locomotion 2.0 (BRAIL 2.0) is a 6-DOF two-legged robot. Each leg has three links: foot link, shank link, and thigh link. The free end of the foot link is the toe. The joint between the foot link and the shank link is the ankle. The joint between the shank link and the thigh link is the knee while that between the two thigh links of the legs is the hip. Each leg has three joints, and each joint has one actuator. The link attached at the hip is the torso link. A weight is attached at the distal end of the torso link. The amount and location of the weight on the torso link are adjustable. The biped has a total of seven links. BRAIL 2.0 cannot bend in the frontal plane as it does not have any “roll” DOF in its legs. BRAIL’s motion is restricted to the sagittal plane, thus making it a planar robot.

The biped jumping motion is studied with respect to the ground or any other flat surface in the sagittal plane (see Fig. 1). The world coordinate system (X – Y) is fixed and absolute. The

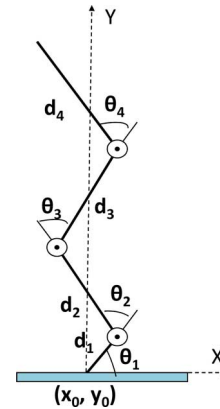


Fig. 1. Biped model.

initial position of the toe is indicated by (x_0, y_0) . The two legs are aligned to have identical pose in the sagittal plane to act as a single leg. In the sagittal plane, the biped has four links and three joints (i.e., active DOFs). The Cartesian coordinates of the ankle, knee, and hip joints are (x_1, y_1) , (x_2, y_2) , and (x_3, y_3) with respect to X – Y . The body angular coordinate vector $\theta_b = (\theta_2, \theta_3, \theta_4)^T$ describes the shape of the biped. The relative angles $(\theta_2, \theta_3, \theta_4)$ are known as *shape variables* and are achieved by an actuator in each leg. As a consequence, each DOF consists of two actuators placed at the same location of the two legs in the sagittal plane. θ_1 is the absolute angle between the foot and the ground. The vector of generalized coordinates $\theta_a := (\theta_1, \theta_b^T)^T$ indicates the absolute posture of the biped. Angles are positive in the counterclockwise direction. The lengths and masses of the foot, shank, thigh, and torso links are d_i and m_i (with $i = 1, 2, 3, 4$), respectively.

The mechanical design is built at Autodesk Inventor (usa.autodesk.com). The Autodesk design and the biped BRAIL 2.0 are shown in Fig. 2. The biped weighs 1.37 kg and is 0.451 m high. The biped model, which is developed at Autodesk Inventor, is imported to Msc. Visualnastran (www.mssoftware.com) simulation environment. The biped parameters in Table I are collected from the Msc. Visualnastran simulation environment and are used in the computation of dynamics.

1) *Actuators*: The RX-64 motors from Robotis, Inc. (www.robotis.com) are used as actuators. The motors weigh 116 g and provide a maximum torque of 6.4 N·m. With two actuators at each joints in the sagittal plane, the maximum torque available at any joint is 12.8 N·m. These actuators are run in “endless turn”/torque control mode. While controlling torque, the torque input to the motor can be adjusted at a resolution of about 0.1% of the maximum available torque at the current supply voltage. The actuators provide angular positions, velocities, and joint torques as feedback.

2) *Controller*: The motors are controlled using a CM2 controller board (www.robotis.com). The CM2 board uses an ATmega128 16 MHz processor. The controller can be connected to the PC using an RS232 port through which HEX code, which is generated from C programs, is downloaded. A unique ID is set for each actuator for the controller to communicate with them. The motors utilize the RS-485 communication protocol to use

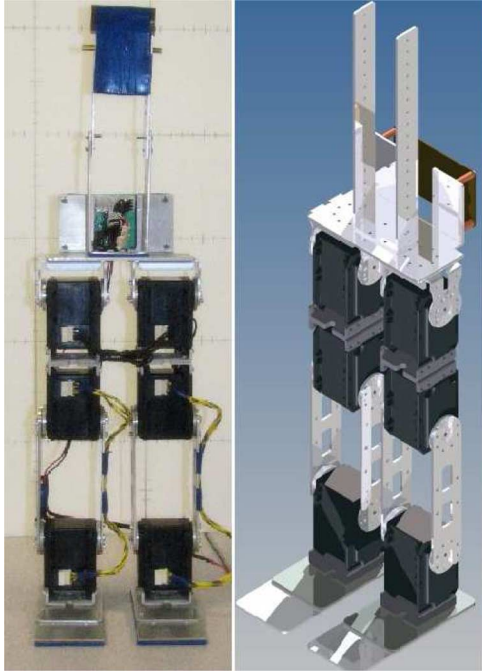


Fig. 2. BRAIL 2.0 and Autodesk design.

TABLE I
PARAMETERS OF THE BIPED

Link	Length (m)	Mass (kg)	CM (m)	Inertia about CM (kgm^2)
1	$d_1=0.12$	$m_1 = 0.32^a$	0.085	4.56×10^{-5}
2	$d_2=0.1$	$m_2 = 0.13^a$	0.05	4.6×10^{-5}
3	$d_3=0.107$	$m_3 = 0.61^a$	0.0535	3.65×10^{-4}
4	$d_4=0.19$	$m_4=0.31$	0.17	2.88×10^{-4}

^a $m_1/m_2/m_3$: Sum of the Foot/Shank/Thigh masses in the two legs.

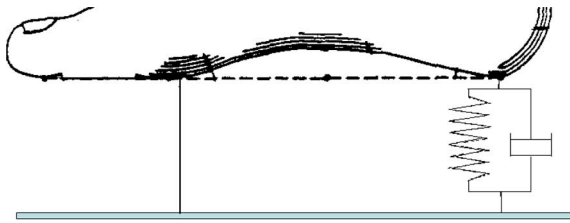


Fig. 3. Foot compliance model.

the daisy chain technology. The controller can read the joint angular positions, velocities, and torques of the each actuator connected in the daisy chain.

B. Foot Compliance Model and Foot Design

The foot-ground compliance model is shown in Fig. 3 by replacing the foot link with a human foot. The entire contact surface between the foot and the ground is represented by a pivot and a spring-damper system located at the toe and the ankle, respectively.

The assumptions on the foot compliance model are as follows.

- C1) When the foot is flat, the entire foot-ground contact surface is represented by the contacts at the toe and ankle.



Fig. 4. Foot plate of BRAIL 2.0.

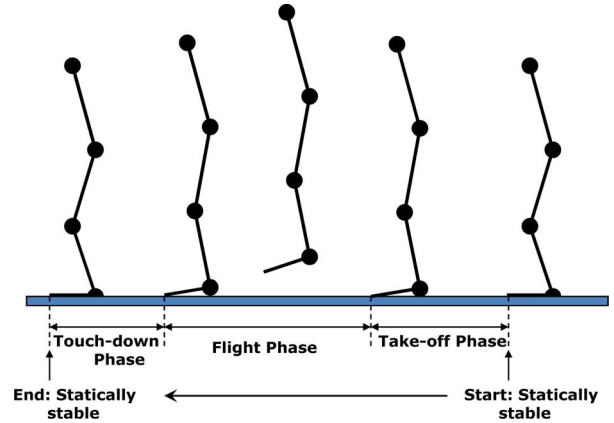


Fig. 5. Phases of jumping motion.

- C2) The toe-ground contact acts as a rigid pivot and the biped does not slip, rebound, or penetrate at this point, i.e., the vertical component of the GRF is positive and the ratio of the horizontal component to the vertical component does not exceed the coefficient of static friction [6], [7], [34].
- C3) The ankle-ground contact acts as a spring-damper system where the biped can rebound or penetrate.

The foot link of BRAIL 2.0 is shown in Fig. 4. Foot bottoms are cushioned by rubber sheets. The rubber cushioning helps to avoid slipping and provides damping to help shock absorption during jumping. The foot link has two plates connected together at ankle while the toe part has only one plate. This makes the ankle-ground joint better damped and stronger to absorb impacts during landing.

C. Jumping Sequences

The jumping process is divided into three phases: takeoff phase, flight phase, and touchdown phase (see Fig. 5). The biped's absolute position is specified by the Cartesian coordinates of CM (x_{CM}, y_{CM}) with respect to the world coordinate frame $X-Y$. In the takeoff phase, the foot link is in contact with the ground and $\dot{y}_{CM} > 0$. The biped is said to be in the touch-down phase when the foot link is in contact with the ground and $\dot{y}_{CM} < 0$. There is no contact with the ground in the flight phase.

At the time of initiation of the flight phase, $\dot{y}_0 > 0$. In the flight phase, the biped's CM evolves according to Newton's second law

$$\begin{aligned} \ddot{x}_{CM} &= 0 \\ \ddot{y}_{CM} &= -g. \end{aligned} \tag{1}$$

In the takeoff and touchdown phases, the CM $[x_{\text{CM}}(\theta_a), y_{\text{CM}}(\theta_a)]$ of the biped can be computed with respect to the toe position

$$\begin{aligned} x_{\text{CM}}(\theta_a) &= \frac{\sum_{i=1}^4 m_i x_{\text{CM}i}}{\sum_{i=1}^4 m_i} \\ y_{\text{CM}}(\theta_a) &= \frac{\sum_{i=1}^4 m_i y_{\text{CM}i}}{\sum_{i=1}^4 m_i} \\ f_{\text{CM}}(\theta_a) &= \begin{bmatrix} x_{\text{CM}}(\theta_a) \\ y_{\text{CM}}(\theta_a) \end{bmatrix} \end{aligned} \quad (2)$$

where m_i and $(x_{\text{CM}i}, y_{\text{CM}i})$ indicate the mass and position of the CM of the i th link, respectively. Therefore, the linear velocity of the biped's CM (with respect to the toe) is given by

$$\begin{bmatrix} \dot{x}_{\text{CM}}(\theta_a) \\ \dot{y}_{\text{CM}}(\theta_a) \end{bmatrix} = \frac{\partial f_{\text{CM}}(\theta_a)}{\partial \theta_a} \dot{\theta}_a. \quad (3)$$

While standing statically on flat foot in the sagittal plane, the biped is statically stable if condition (4) is satisfied [1]

$$0 \leq x_{\text{CM}}(\theta_a) \leq \text{foot length} = d_1. \quad (4)$$

Without loss of generality, it is assumed that the jumping motion starts from a statically stable posture with the origin of the world coordinate system coinciding with the position of the toe. The toe is in contact with the ground in both the takeoff and touchdown phases, and the toe-ground contact acts as a rigid pivot during these phases. Impact occurs when the toe touches the ground soon after the flight phase or just before the touchdown phase. Due to the impact, the joint angular velocities change instantaneously while the joint angular positions remain unchanged. The desired gaits in three jumping phases are computed offline ensuring landing stability. Stability of the jumping gaits depends on the biped dynamics and control strategies. The control strategies ensure asymptotic convergence to a statically stable posture at the end of the touchdown phase.

D. Lagrangian Dynamics During Takeoff and Touchdown Phases

The biped's dynamic model during takeoff and touchdown phases are obtained using Lagrangian formulation [26] based on the biped parameters in Table I. The biped dynamics have the following form:¹

$$M_s(\theta_b) \ddot{\theta}_a + V_s(\theta_a, \dot{\theta}_a) + G_s(\theta_a) = \tau_s \quad (5)$$

where M_s is the 4×4 inertial matrix about the toe, V_s is the 4×1 vector containing the Coriolis and centrifugal terms, and G_s is the 4×1 gravity vector. τ_s is the vector of the generalized forces and torques applied to the biped. The external torques are¹

$$\tau_s = \begin{bmatrix} \tau_1 \\ \tau_2 \\ \tau_3 \\ \tau_4 \end{bmatrix} = B_{\bar{t}s} u_t + B_{bs} u_s \quad (6)$$

¹“s” stands for the takeoff and touchdown phase, “f” for the flight phase, “b” for shape variables, “a” for absolute orientation, and “t” for toe-ground joint.

where $u_s = [\tau_2 \ \tau_3 \ \tau_4]^T$ are the torques applied by the ankle, knee, and waist actuators, respectively. $u_t = \tau_1$ is the torque generated about the toe-ground contact point due to the GRFs at the ankle-ground contact point

$$\tau_1 = \begin{cases} -kd_1^2 \theta_1 - Dd_1^2 \dot{\theta}_1, & \text{when } \theta_1 \leq 0 \\ 0, & \text{otherwise} \end{cases} \quad (7)$$

where k and D are the spring constant and damping of the ankle-ground contact, and

$$B_{\bar{t}s} = \begin{bmatrix} 1 \\ 0 \\ 0 \\ 0 \end{bmatrix} \quad B_{bs} = \begin{bmatrix} 0 & 0 & 0 \\ 1 & 0 & 0 \\ 0 & 1 & 0 \\ 0 & 0 & 1 \end{bmatrix}. \quad (8)$$

Introducing the state vector $x_s := (\theta_a^T, \dot{\theta}_a^T)^T$, the Lagrangian model (5) is expressed as

$$\begin{aligned} \dot{x}_s &= \begin{bmatrix} \dot{\theta}_a \\ M_s^{-1}(-V_s - G_s + B_{\bar{t}s} u_t) \end{bmatrix} + \begin{bmatrix} 0 \\ M_s^{-1} B_{bs} u_s \end{bmatrix} \\ &= f_s(x_s) + g_s(x_s) u_s \end{aligned} \quad (9)$$

where $x_s \in \Delta_s$, $\Delta_s := \{x_s = (\theta_a^T, \dot{\theta}_a^T)^T \mid y_0 = 0, y_1 \geq 0, y_2 > 0, y_3 > 0, y_4 > 0, \theta_a \in \mathbb{R}^4\}$.

E. Lagrangian Dynamics During Flight Phase

For flight phase, the generalized vector coordinates are considered as $\theta_f := (\theta_1, \theta_b^T, x_{\text{CM}}, y_{\text{CM}})^T$. The flight phase dynamics are given by¹

$$D_f(\theta_b) \ddot{\theta}_f + V_f(\theta_f, \dot{\theta}_f) + G_f(\theta_f) = \tau_f \quad (10)$$

where V_f is the 6×1 vector containing the Coriolis and centrifugal terms, G_f is the 6×1 gravity vector, and D_f is given by

$$D_f = \begin{bmatrix} M_f(\theta_b) & 0_{4 \times 2} \\ 0_{2 \times 4} & mI_{2 \times 2} \end{bmatrix} \quad (11)$$

where $I_{2 \times 2}$ is the 2×2 unity matrix and $M_f(\theta_b)$ is the inertial matrix of the biped about the CM, which is given by [6]

$$M_f(\theta_b) = M_s(\theta_b) - m \frac{\partial f_{\text{CM}}(\theta_a)^T}{\partial \theta_a} \frac{\partial f_{\text{CM}}(\theta_a)}{\partial \theta_a}. \quad (12)$$

The external torques are

$$\tau_f = \begin{bmatrix} 0 \\ \tau_2 \\ \tau_3 \\ \tau_4 \\ 0 \\ 0 \end{bmatrix} = B_{af} u_f \quad B_{af} = \begin{bmatrix} 0 & 0 & 0 \\ 1 & 0 & 0 \\ 0 & 1 & 0 \\ 0 & 0 & 1 \\ 0 & 0 & 0 \\ 0 & 0 & 0 \end{bmatrix} \quad (13)$$

where $u_f = [\tau_2 \ \tau_3 \ \tau_4]^T$ are the torques applied by the ankle, knee, and waist actuators, respectively, during the flight phase.

Introducing the state vector $x_f := (\theta_f^T, \dot{\theta}_f^T)^T$, the model (10) becomes

$$\begin{aligned} \dot{x}_f &= \begin{bmatrix} \dot{\theta}_f \\ D_f^{-1}(-V_f - G_f) \end{bmatrix} + \begin{bmatrix} 0 \\ D_f^{-1}B_{af}u_f \end{bmatrix} \\ &= f_f(x_f) + g_f(x_f)u_f \end{aligned} \quad (14)$$

where $x_f \in \Delta_f$, $\Delta_f := \{x_f = (\theta_f^T, \dot{\theta}_f^T)^T \mid y_0 > 0, y_1 > 0, y_2 > 0, y_3 > 0, y_4 > 0, \theta_f \in \mathcal{R}^6\}$.

F. Impact Model and Angular Momentums

The impact takes place when the toe touches the ground at the end of the flight phase. The impact model is assumed nonelastic and instantaneous with the velocity of the toe becoming zero instantaneously leading to discontinuity in joint velocities [25]. As the impact is assumed instantaneous, it can be treated as an impulsive-dynamics event. Thus, the biped's configuration is assumed constant and the position vector (θ_a) does not change during the impact interval. The toe-ground contact acts as an ideal pivot after the impact. The positions and velocities just before and after the impact are denoted by “-” and “+,” respectively. Using the model in [25], the joint velocities just after impact are obtained by

$$\dot{\theta}_a^+ = M_s(\theta_b^-)^{-1} \left[M_f(\theta_b^-); m \frac{\partial f_{CM}(\theta_a^-)^T}{\partial \theta_a^-} \right] \dot{\theta}_f^-. \quad (15)$$

In takeoff and touchdown phases, the angular momentum of the biped about the toe is given by² [6]

$$\sigma = M_{s,1} \dot{\theta}_a. \quad (16)$$

The angular momentum after the impact is computed by the following equation:

$$\sigma^+ = M_{s,1}(\theta_a^+) \dot{\theta}_a^+. \quad (17)$$

III. CONTROL LAW DEVELOPMENT

The control law for all the phases is formulated as an *output zeroing* problem resulting in nontrivial ZD [10]. The output functions for all the three phases are defined as

$$h(\theta_b, t) = \theta_b - \theta_b^d(t) \quad (18)$$

where $\theta_b^d(t)$ is the vector of three desired shape variable trajectories. The desired trajectories in takeoff, flight, and touchdown phases are $\theta_{bs}^d(t)$, $\theta_{bf}^d(t)$, and $\theta_{bl}^d(t)$, respectively.

From (18), the following equations can be derived:³

$$\begin{aligned} \dot{h}(\theta_b, t) &= \frac{\partial h}{\partial x} \dot{x} - \dot{\theta}_b^d(t) = L_F h - \dot{\theta}_b^d(t) \\ \ddot{h}(\theta_b, t) &= (L_G L_F h)u + L_F^2 h - \ddot{\theta}_b^d(t) \end{aligned} \quad (19)$$

where F , G , and x are from the system equations (9) and (14). F , G , and x are f_s , g_s , and x_s for takeoff and touchdown phases

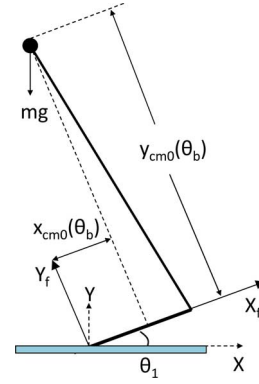


Fig. 6. Two-link equivalent model of the biped with foot.

and f_f , g_f , and x_f for the flight phase. The feedback controller is defined as

$$\begin{aligned} u(x) &= [L_G L_F h]^{-1} [v(h, L_F h) - L_F^2 h + \ddot{\theta}_b^d(t)] \\ v(h, L_F h) &= -K_d(\dot{\theta}_b - \dot{\theta}_b^d(t)) - K_p(\theta_b - \theta_b^d(t)) \end{aligned} \quad (20)$$

where K_d and K_p are constants such that $\ddot{h} + K_d \dot{h} + K_p h = 0$ is stable.

IV. SELECTION OF DESIRED GAITS

The selection of the desired gaits⁴ $[\theta_{bs}^d(t), \theta_{bf}^d(t), \text{ and } \theta_{bl}^d(t)]$ is discussed in this section. The selection procedure is based on the equivalent two-link model of the biped (see Fig. 6). In the two-link model, the foot link acts as one link, and the distance from the ankle to CM of the rest of the biped acts as another link. The Cartesian coordinate $(x_{CM0}(\theta_b), y_{CM0}(\theta_b))$ is as per Fig. 6 [with respect to the coordinate system (X_f, Y_f)]. Considering the mechanical structure of the biped, i.e., BRAIL 2.0, its physically reasonable configurations correspond to θ_b (in radians) in the ranges $1.8408 \leq \theta_2 \leq 3.1227$, $-2.7585 \leq \theta_3 \leq -0.5219$, and $0.2066 \leq \theta_4 \leq 1.2519$.

The desired gaits $\theta_b^d(t)$ are computed from the desired trajectories of $(x_{CM0}(\theta_b), y_{CM0}(\theta_b))$ in various phases using MATLAB's LSQNONLIN function that utilizes the trust-region method [29] for nonlinear error minimization of the following function:

$$\Gamma(\theta_b^d) = (x_{CM0}^d(t) - x_{CM0}(\theta_b^d))^2 + (y_{CM0}^d(t) - y_{CM0}(\theta_b^d))^2 \quad (21)$$

where $(x_{CM0}^d(t), y_{CM0}^d(t))$ is the desired Cartesian trajectory of $(x_{CM0}(\theta_b), y_{CM0}(\theta_b))$. The nonlinear error minimization on (21) is performed with the constraints that the solution vectors θ_b^d lie within the ranges of the physically reasonable configurations of the biped. Subsequently, a fourth-order polynomial is considered to fit the set of solutions obtained from the nonlinear error minimization of (21). The fourth-order polynomial resulted in error in the order of 10^{-4} m

$$\theta_j^d(t) = a_{j,0} + a_{j,1}t + a_{j,2}t^2 + a_{j,3}t^3 + a_{j,4}t^4. \quad (22)$$

⁴"r" stands for the landing phase or touchdown phase.

² $M_{s,r}$ indicates the r th row of the stance-phase inertia matrix.

³See [10] for Lie algebraic notations.

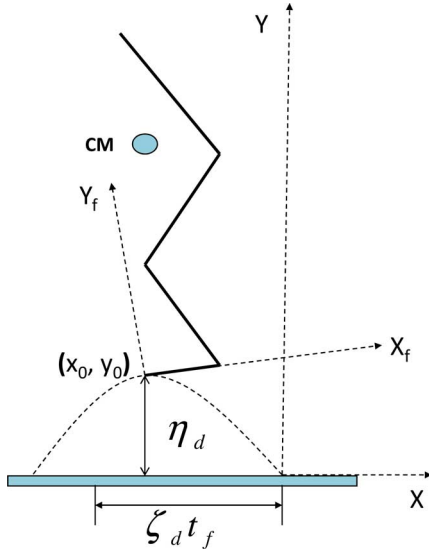


Fig. 7. Flight phase gait design parameters.

With $\theta_j^d(t)$ in (22), $(x_{CM0}(\theta_b), y_{CM0}(\theta_b))$ closely follows $(x_{CM0}^d(t), y_{CM0}^d(t))$.

A. Takeoff Phase Gait

In the takeoff phase, $(x_{CM0}^d(t), y_{CM0}^d(t))$ is given by⁵

$$\begin{aligned} x_{CM0}^d(t) &= x_{CM0}(0) - C_x t \\ y_{CM0}^d(t) &= y_{CM0}(0) + C_y t \end{aligned} \quad (23)$$

where $(x_{CM0}(0), y_{CM0}(0))$ is the initial location of $(x_{CM0}(\theta_b), y_{CM0}(\theta_b))$. C_x and C_y are the desired horizontal and vertical takeoff velocities. $(x_{CM0}^d(t), y_{CM0}^d(t))$ should be such that $\theta_a := (0, (\theta_b^d)^T)^T$ is real.

B. Flight Phase Gait

The biped's CM evolves according to (1) in the flight phase. The shape variables are adjusted to vary the CM position with respect to the toe (x_0, y_0) . The desired trajectory $y_{CM0}^d(t)$ is given by

$$\begin{aligned} y_{CM}(t) &= y_{CM}(0) + \dot{y}_{CM}(0)t - \frac{1}{2}gt^2 \\ y_0^d(t) &= \eta^d \sin\left(\frac{\pi}{t_f}t\right) \\ y_{CM0}^d(t) &= y_{CM}(t) - y_0^d(t) \end{aligned} \quad (24)$$

where η^d is the desired jumping height, t_f is the desired flight time, and $y_0^d(t)$ is the desired trajectory of y_0 (see Fig. 7). Similarly, the desired trajectory of $x_{CM0}^d(t)$ is given by

$$\begin{aligned} x_{CM}(t) &= x_{CM}(0) + \dot{x}_{CM}(0)t \\ x_0^d(t) &= \zeta^d t \\ x_{CM0}^d(t) &= x_{CM}(t) - x_0^d(t) \end{aligned} \quad (25)$$

⁵Negative sign appears in the expression of $x_{CM0}^d(t)$ because x is negative in the forward direction of jumping.

where ζ^d is the desired length of jumping and $x_0^d(t)$ is the desired trajectory of x_0 (see Fig. 7). The values of $x_{CM}(0)$, $\dot{x}_{CM}(0)$, $y_{CM}(0)$, and $\dot{y}_{CM}(0)$ are their values at the end of the takeoff phase. η^d , ζ^d , and t_f should be chosen such that $\theta_1 > 0$ at the end of the flight phase.

C. Touchdown Phase Gait

The initial positions in the touchdown phase are the positions at the end of the flight phase while the initial velocities change instantaneously according to (15) due to impact at the end of the flight phase. The desired shape variables $\theta_j^d(t)$ ($j = 2, 3, 4$) during the touchdown phase are constants

$$\theta_j^d(t) = \text{constant} \quad (26)$$

such that $0 < x_{CM0}(\theta_{bl}^d) < d_1 = \text{foot length}$ and $\theta_j^d(t) = 0$.

V. LANDING STABILITY ANALYSIS

Landing stability is ensured by biped's asymptotic convergence to a statically stable posture. The control law (20) results in nontrivial ZD in the touchdown phase [10]. Stability of the closed-loop dynamics (CLD) is governed by the touchdown phase ZD.

A. Switching Zero Dynamics (SZD): Touchdown Phase

The ZD manifold in touchdown phase with the output function (18) is given by [10]

$$Z_s := \{x_s \in \Delta_s \mid \theta_b = \theta_b^d(t), \dot{\theta}_b = \dot{\theta}_b^d(t)\}. \quad (27)$$

The ZD (27) leads to (28) with desired shape trajectories according to (26) [7]⁶

$$\begin{aligned} \dot{\theta}_1 &= \frac{\sigma}{M_{s,1,1}(\theta_{bl}^d)} \\ \dot{\sigma} &= -mgx_{CM}(\theta_1, \theta_{bl}^d) + \tau_1. \end{aligned} \quad (28)$$

The variable $x_{CM}(\theta_a)$ [27] has the following form:

$$\begin{aligned} x_{CM}(\theta_a) &= -\sqrt{x_{CM0}^2(\theta_b) + y_{CM0}^2(\theta_b)} \\ &\quad \times \sin\left(\theta_1 - \tan^{-1}\left(\frac{x_{CM0}(\theta_b)}{y_{CM0}(\theta_b)}\right)\right). \end{aligned} \quad (29)$$

The variable M_s is independent of θ_1 and $M_{s,1,1}(\theta_{bl}^d)$ in (28) is a constant. Let us define three positive constants as follows:

$$\begin{aligned} K_1 &= \frac{1}{M_{s,1,1}(\theta_{bl}^d)} \text{ kg}^{-1} \cdot \text{m}^{-2} \\ K_2 &= mg\sqrt{x_{CM0}^2(\theta_{bl}^d) + y_{CM0}^2(\theta_{bl}^d)} \text{ N} \cdot \text{m} \\ K_3 &= \tan^{-1}\left(\frac{x_{CM0}(\theta_{bl}^d)}{y_{CM0}(\theta_{bl}^d)}\right) \text{ rad}. \end{aligned} \quad (30)$$

⁶ $M_{s,r,c}$ indicates the element in the r th row and c th column of the stance-phase inertia matrix.

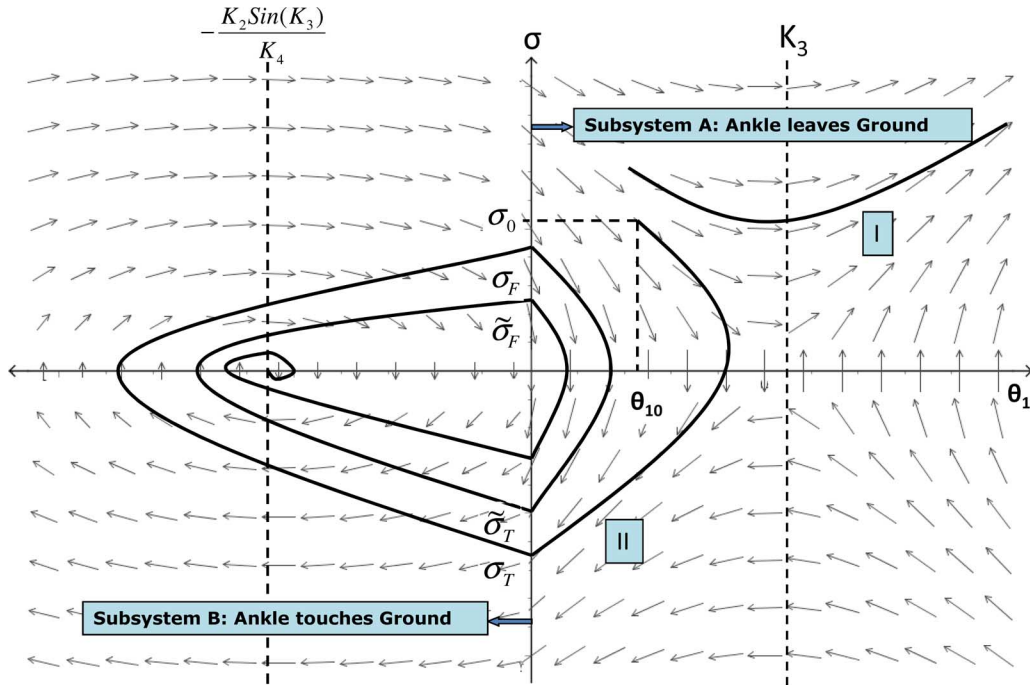


Fig. 8. Phase portrait of SZD (31). Trajectory I: Member of the set of trajectories going out with increasing θ_1 . Trajectory II: Member of the set of trajectories reaching the $\theta_1 = 0$ plane. The first switching occurs at $(0, \sigma_T)$ from subsystem A to subsystem B. The second switching occurs at $(0, \sigma_F)$ from subsystem B to subsystem A. The third switching occurs at $(0, \tilde{\sigma}_T)$ from subsystem A to subsystem B. The fourth switching occurs at $(0, \tilde{\sigma}_F)$ from subsystem B to subsystem A.

Thus, the ZD in (28) becomes

$$\begin{aligned}\dot{\theta}_1 &= K_1 \sigma \\ \dot{\sigma} &= K_2 \sin(\theta_1 - K_3) + \tau_1.\end{aligned}\quad (31)$$

The initial value of θ_1 in the touchdown phase is positive and is given by its value at the end of the flight phase. The value of σ changes on impact and its values after the impact σ^+ is computed from (17). The torque at the toe-ground contact τ_1 in (7) is written as

$$\tau_1 = \begin{cases} -K_4 \theta_1 - K_5 \sigma, & \text{when } \theta_1 \leq 0 \\ 0, & \text{otherwise} \end{cases}\quad (32)$$

where $K_4 = kd_1^2$ N-m and $K_5 = Dd_1^2 K_1 s^{-1}$. K_4 indicates the stiffness properties of the ankle-ground contact. The value of k is on the order of 10^6 N/m for soft surfaces [33], leading to K_4 on the order of 10^4 N-m. The value of D is generally 5%–25% of k making K_5 on the order of 10^2 s⁻¹. The ZD in (31) has two equilibrium points in the range $-\pi < \theta_1 < \pi$: $(\theta_1, \sigma) = (K_3, 0)$ and $(\theta_1, \sigma) \approx (-(K_2 \sin(K_3)/K_4), 0)$.⁷ $(-(K_2 \sin(K_3)/K_4), 0)$ corresponds to statically stable posture where $K_2 \sin(K_3)/K_4 \approx 0$ as the value of K_4 is quite high compared with K_2 .

The phase portrait of the ZD (31) shows that the touchdown phase ZD is a switching system with two subsystems (see Fig. 8): subsystem A (33) for $\theta_1 > 0$ and subsystem B (34) for $\theta_1 \leq 0$. Switching takes place whenever the ankle touches or leaves the

⁷ θ_1 is small compared with K_3 in subsystem B, i.e., $\sin(\theta_1 - K_3) \approx -\sin(K_3)$.

ground. The overall ZD during the touchdown phase is named SZD.

In subsystem A ($\theta_1 > 0$), the touchdown phase ZD is given by

$$\begin{aligned}\dot{\theta}_1 &= K_1 \sigma \\ \dot{\sigma} &= K_2 \sin(\theta_1 - K_3).\end{aligned}\quad (33)$$

In subsystem B ($\theta_1 \leq 0$), the touchdown phase ZD is given by

$$\begin{aligned}\dot{\theta}_1 &= K_1 \sigma \\ \dot{\sigma} &= K_2 \sin(\theta_1 - K_3) - K_4 \theta_1 - K_5 \sigma.\end{aligned}\quad (34)$$

The touchdown phase always begins in subsystem A. For the SZD to be stable, it needs to converge asymptotically to the equilibrium $(\theta_1, \sigma) = (-(K_2 \sin(K_3)/K_4), 0)$.

B. Stability of SZD

Stability analysis of SZD consists of three aspects: 1) In subsystem A (see Fig. 8), the phase portrait can either follow trajectory I or II. Trajectory I leads to instability of the biped structure. For trajectory II, switching takes place at the $\theta_1 = 0$ plane, which is required for stability of the ZD. 2) For stability in subsystem B, the ZD should either converge to the equilibrium point $(\theta_1, \sigma) = (-(K_2 \sin(K_3)/K_4), 0)$, or it should switch back to subsystem A. The possibility of initiating a flight phase from subsystem B is not addressed here as the biped is not

supposed to rebound at the toe–ground contact according to the assumption C2) of the foot compliance model. 3) The switching should be such that the SZD asymptotically converges to the equilibrium point $(\theta_1, \sigma) = (-(K_2 \sin(K_3)/K_4), 0)$.

In the following analysis, it is assumed that SZD (31) starts at (θ_{10}, σ_0) , with $\theta_{10} > 0$ being the value of θ_1 at the end of the flight phase, and σ_0 is computed from (17).

Theorem 1: The SZD (33) reaches the $\theta_1 = 0$ plane from the initial states (θ_{10}, σ_0) if the following condition is satisfied ($\theta_{10} > 0$).

1) When $K_3 > \theta_{10}$

$$\text{ZD1: } \sigma_0 < \sqrt{\frac{2K_2}{K_1}(1 - \cos(\theta_{10} - K_3))}.$$

2) When $K_3 \leq \theta_{10}$

$$\text{ZD1: } \sigma_0 < -\sqrt{\frac{2K_2}{K_1}(1 - \cos(\theta_{10} - K_3))}.$$

Proof: The proof is given in Appendix I. ■

Theorem 2: The SZD (34) is locally asymptotically stable with initial states $(0, \sigma_T)$ if the following condition is satisfied:

$$\text{ZD2: } \frac{\sigma_T^2}{2 \int_B \sigma^2 dt} > K_5 > 0$$

where “ B ” indicates the time interval when the solution vector of (31) is in subsystem B.

Proof: The proof is given in Appendix II. ■

The SZD (31) is a switching system and switching occurs at the $\theta_1 = 0$ plane. Condition ZD1 ensures that (33) reaches the $\theta_1 = 0$ plane. Condition ZD2 ensures (34) either converges to the stable equilibrium $(-(K_2 \sin(K_3)/K_4), 0)$ or switches back to subsystem A. However, the switching points $(0, \sigma_F)$ or $(0, \tilde{\sigma}_F)$ to subsystem A might not satisfy ZD1, thus leading to instability. Therefore, conditions ZD1 and ZD2 are not sufficient to ensure the stability of SZD (31).

Theorem 3: The SZD (31) locally asymptotically converges to the equilibrium point $(-(K_2 \sin(K_3)/K_4), 0)$ from initial states (θ_{10}, σ_0) if the following conditions are satisfied:

$$\text{SZD1: } K_3 > \theta_{10} > 0.$$

$$\text{SZD2: } |\sigma_0| < \sqrt{\frac{2K_2}{K_1}(1 - \cos(\theta_{10} - K_3))}.$$

$$\text{SZD3: } \text{ZD2}.$$

Proof: The proof is given in Appendix III. ■

The stability of SZD (31) depends on the initial states. The initial states of the SZD are the values at the CLD when $h(\theta_b, t) = 0$ and $\dot{h}(\theta_b, t) = 0$. Hence, stability of SZD is dependent on that of the CLD and *vice versa*.

C. CLD: Touchdown Phase

CLD in both takeoff and touchdown phases is given by

$$\begin{aligned} \ddot{h} + K_d \dot{h} + K_p h &= 0 \\ \dot{\theta}_1 &= \frac{\sigma}{M_{s,1,1}} - \frac{M_{s,1,2}}{M_{s,1,1}} \dot{\theta}_2 - \frac{M_{s,1,3}}{M_{s,1,1}} \dot{\theta}_3 - \frac{M_{s,1,4}}{M_{s,1,1}} \dot{\theta}_4 \\ \dot{\sigma} &= -mg x_{\text{CM}}(\theta_a) + \tau_1. \end{aligned} \quad (35)$$

In the touchdown phase, the CLD leads to (36) with the control input (20) and desired gait (26)

$$\begin{aligned} \dot{\xi}_1 &= \xi_2 \\ \dot{\xi}_2 &= -\frac{K_P}{\epsilon^2} \xi_1 - \frac{K_D}{\epsilon} \xi_2 \\ \dot{\theta}_1 &= \kappa_1(\xi_1) \sigma - \kappa_4(\xi_1) \xi_2 \\ \dot{\sigma} &= \kappa_2(\xi_1) \sin(\theta_1 - \kappa_3(\xi_1)) + \tau_1 \end{aligned} \quad (36)$$

where ϵ is a small positive constant, $K_p = K_P/\epsilon^2$, and $K_d = K_D/\epsilon$, with K_P and K_D being constant gains. ϵ acts as the perturbation parameter [28], and the significance of ϵ is explored in the Appendix in the proof of Theorem 4. ξ_1 , ξ_2 , $\kappa_1(\xi_1)$, $\kappa_2(\xi_1)$, $\kappa_3(\xi_1)$, and $\kappa_4(\xi_1)$ are given by

$$\begin{aligned} \xi_1 &= h(\theta_b, t) = \theta_b - \theta_{bl}^d \\ \xi_2 &= \dot{h}(\theta_b, t) = \dot{\theta}_b \\ \kappa_1(\xi_1) &= \frac{1}{M_{s,1,1}(\xi_1)} \\ \kappa_2(\xi_1) &= mg \sqrt{(x_{\text{CM}0}^2(\xi_1) + y_{\text{CM}0}^2(\xi_1))} \\ \kappa_3(\xi_1) &= \tan^{-1} \left(\frac{x_{\text{CM}0}(\xi_1)}{y_{\text{CM}0}(\xi_1)} \right) \\ \kappa_4(\xi_1) &= \begin{bmatrix} M_{s,1,2} & M_{s,1,3} & M_{s,1,4} \\ M_{s,1,1} & M_{s,1,1} & M_{s,1,1} \end{bmatrix}. \end{aligned} \quad (37)$$

Lemma 1: Consider the CLD (36). $\kappa_3(\xi_1) > \theta_1$ implies $x_{\text{CM}}(\theta_a) > 0$, and $\kappa_3(\xi_1) \leq \theta_1$ implies $x_{\text{CM}}(\theta_a) \leq 0$.

Proof: Using (37), $\kappa_3(\xi_1) = \tan^{-1}(x_{\text{CM}0}(\xi_1)/y_{\text{CM}0}(\xi_1))$

$$\begin{aligned} \kappa_3(\xi_1) &= \tan^{-1} \left(\frac{x_{\text{CM}0}(\xi_1)}{y_{\text{CM}0}(\xi_1)} \right) > \theta_1 \\ \implies \sin(\theta_1) y_{\text{CM}0}(\xi_1) - \cos(\theta_1) x_{\text{CM}0}(\xi_1) &< 0 \\ \implies \frac{\kappa_2(\xi_1)}{mg} \sin(\kappa_3(\xi_1) - \theta_1) &> 0 \text{ [using (37)]} \\ \implies x_{\text{CM}}(\theta_a) &> 0 \text{ [using (29)].} \end{aligned}$$

Hence, $\kappa_3(\xi_1) > \theta_1$ implies $x_{\text{CM}}(\theta_a) > 0$, and similarly, $\kappa_3(\xi_1) \leq \theta_1$ implies $x_{\text{CM}}(\theta_a) \leq 0$. ■

The last two equations in (36) of $\dot{\theta}_1$ and $\dot{\sigma}$ are known as the *internal dynamics* of the system. Let us define $\psi = \theta_1 + \int \kappa_4(\xi_1) d\xi_1$. From (36) in subsystem A ($\theta_1 > 0$)

$$\begin{aligned} \frac{d\sigma}{d\psi} &= \frac{\kappa_2 \sin(\theta_1 - \kappa_3)}{\kappa_1 \sigma} \\ \sigma d\sigma &= \frac{\kappa_2}{\kappa_1} \sin(\theta_1 - \kappa_3) d\psi \\ \frac{\sigma^2(0)}{2} &= \frac{\sigma^2}{2} + V_{ID}(\theta_1, \xi_1) \end{aligned} \quad (38)$$

where $V_{ID}(\theta_1, \xi_1) = -\int_{\psi_0}^{\psi} (\kappa_2/\kappa_1) \sin(\theta_1 - \kappa_3) d\psi$, and ψ_0 and $\sigma(0)$ are the values of ψ and σ at the beginning of the touchdown phase. $\dot{V}_{ID}(\theta_1, \xi_1) = \kappa_2(\xi_1) \sin(\kappa_3(\xi_1) - \theta_1) \sigma$, and the optimal values of $V_{ID}(\theta_1, \xi_1)$ occur at $\dot{V}_{ID}(\theta_1, \xi_1) = 0$. At $\sigma = 0$, with a specific combination of $\xi_1(0)$, $\xi_2(0)$, K_P , K_D ,

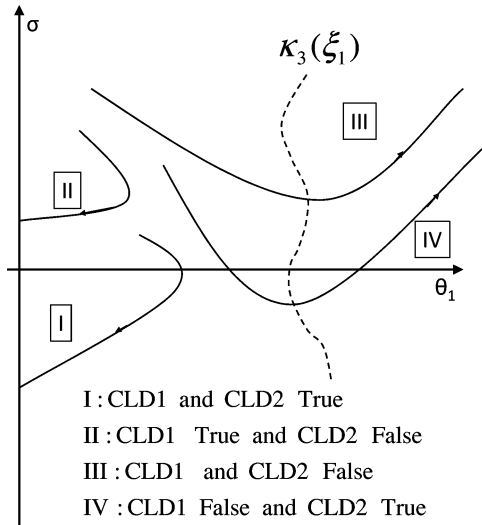


Fig. 9. Stability of internal dynamics.

and ϵ at the $\theta_1 = \theta_1(0)$ plane, $V_{ID}(\theta_1, \xi_1)$ is maximum [from (38)], and the maximum value is equal to $\sigma^2(0)/2$. Such maximum values of $V_{ID}(\theta_1, \xi_1)$ vary depending on the initial angular momentum $\sigma(0)$ during landing. There is a minimum value of $\sigma(0)$ below which the trajectory reaches the $\sigma = 0$ plane (trajectories I and IV in Fig. 9). In other words, there is a maximum value of $\sigma(0)$ above which the trajectory does not reach the $\sigma = 0$ plane (trajectories II and III in Fig. 9). The maximum values of $V_{ID}(\theta_1, \xi_1)$ corresponding to the maximum value of $\sigma(0)$ for which the trajectory reaches the $\sigma = 0$ plane indicate the restriction on the biped's joint angular velocities for stable landing and is named the *critical kinetic index* in Definition 1.

Definition 1: Consider the CLD (36) when $\theta_1(0) < \kappa_3(\xi_1)$. For a specific combination $\xi_1(0)$, $\xi_2(0)$, K_P , K_D , and ϵ at the $\theta_1 = \theta_1(0)$ plane, the value of V_{ID} corresponding to the maximum value of $\sigma(0)$ for which the trajectory reaches the $\sigma = 0$ plane is named the *critical kinetic index*.

Critical kinetic index is denoted by V_{ID}^{\max} . Numerically, V_{ID}^{\max} is found by identifying the maximum touchdown phase initial angular momentum $\sigma(0)$ for which the trajectory reaches the $\sigma = 0$ plane, and $V_{ID}^{\max} = (\sigma(0))^2/2$.

Equation (3) leads to

$$\begin{aligned}
 \dot{x}_{CM}(\theta_a) &= \frac{\partial x_{CM}(\theta_a)}{\partial \theta_a} \dot{\theta}_a \\
 \implies x_{CM}(\theta_a) \dot{x}_{CM}(\theta_a) &= x_{CM}(\theta_a) \frac{\partial x_{CM}(\theta_a)}{\partial \theta_a} \dot{\theta}_a \\
 \implies \frac{x_{CM}^2(\theta_{a0})}{2} &= \frac{x_{CM}^2(\theta_a)}{2} + V_{x_{CM}}(\theta_1, \xi_1) \quad (39)
 \end{aligned}$$

where $V_{x_{CM}}(\theta_1, \xi_1) = -\int_{\theta_{a0}}^{\theta_a} x_{CM}(\theta_a) (\partial x_{CM}(\theta_a) / \partial \theta_a) \dot{\theta}_a dt$, and $\theta_{a0} = \theta_a(0)$ at the beginning of the touchdown phase. $\dot{V}_{x_{CM}}(\theta_1, \xi_1) = -x_{CM}(\theta_a) (\partial x_{CM}(\theta_a) / \partial \theta_a) \dot{\theta}_a$. At $\theta_1 = \kappa_3(\xi_1)$, $x_{CM}(\theta_a) = 0$, and $\dot{V}_{x_{CM}}(\theta_1, \xi_1) = 0$. Hence, $V_{x_{CM}}(\theta_1, \xi_1)$ is maximum at $\theta_1 = \kappa_3(\xi_1)$ for a specific combination of $\xi_1(0)$, $\xi_2(0)$, K_P , K_D , and ϵ at the plane $\sigma = \sigma(0)$ [from (39)]. Such

maximum values of $V_{x_{CM}}(\theta_1, \xi_1)$ depend on the initial landing posture of the biped, i.e., θ_{a0} or $x_{CM}(\theta_{a0})$. There is a maximum value of $x_{CM}(\theta_{a0})$ above which the trajectory does not reach the $\theta_1 = \kappa_3(\xi_1)$ plane (trajectories I and II in Fig. 9). In other words, there is a minimum value of $\theta_1(0)$ below which the trajectory does not reach the $\theta_1 = \kappa_3(\xi_1)$ plane. The maximum values of $V_{x_{CM}}(\theta_1, \xi_1)$ corresponding to the minimum value of $\theta_1(0)$ for which the trajectory reaches the $\theta_1 = \kappa_3(\xi_1)$ plane indicate the restriction on biped's joint angular positions for stable landing and is named the *critical potential index* in Definition 2.

Definition 2: Consider the CLD (36) when $\theta_1(0) < \kappa_3(\xi_1)$. For a specific combination of $\xi_1(0)$, $\xi_2(0)$, K_P , K_D , and ϵ at the $\sigma = \sigma(0)$ plane, the value of $V_{x_{CM}}$ corresponding to the minimum value of $\theta_1(0)$ for which the trajectory reaches the $\theta_1 = \kappa_3(\xi_1)$ plane is named the *critical potential index*.

Critical potential index is denoted by $V_{x_{CM}}^{\max}$. Numerically, $V_{x_{CM}}^{\max}$ is found by identifying the minimum value of $\theta_1(0)$ for which the trajectory reaches the $\theta_1 = \kappa_3(\xi_1)$ plane, and $V_{x_{CM}}^{\max} = x_{CM}^2(\theta_{a0})/2$.

Theorem 4: Consider the CLD (36) and SZD (31). The local asymptotic stability of the SZD (31) implies the local asymptotic stability of CLD (36) if the following conditions are satisfied:

$$\text{CLD1: } x_{CM}(\theta_{a0}) > \sqrt{2V_{x_{CM}}^{\max}}$$

$$\text{CLD2: } |\sigma(0)| < \sqrt{2V_{ID}^{\max}}$$

$$\text{CLD3: } \frac{\sigma_T^2}{2 \int_B \sigma^2 dt} > K_5 > 0 \text{ and } \epsilon \text{ is small enough to ensure that the internal dynamics closely follow the ZD (31).}$$

Here, “B” indicates the time interval when the solution vector of (36) is in subsystem B.

Proof: The proof is given in Appendix IV. ■

Stability of CLD is dependent on the *critical potential index* and *critical kinetic index*. Their closed-form expressions are zero and $(K_2/K_1)(1 - \cos(\theta_{10} - K_3))$, respectively, when the system is within the Z_s (27) manifold. Hence, using Lemma 1, SZD1 and SZD2 and CLD1 and CLD2 are equivalent stability conditions for SZD and CLD, respectively. ϵ should be small enough to satisfy CLD3 to ensure that CLD1 and CLD2 are held in the case of rebounding at the ankle-ground contact point. The bipedal structure and properties of the foot-ground contact surfaces decide the values of the stability parameters K_1 , K_2 , K_3 , K_4 , and K_5 . Therefore, the stability of SZD depends mostly on the bipedal structure and the properties of foot-ground contact surface. However, stability of the CLD is dependent on the *critical potential index* and *critical kinetic index*, which further depend on design parameters K_P , K_D , and ϵ .

VI. SIMULATIONS AND EXPERIMENTS

A. Jumping Gait Simulations

Simulations are done based on the parameters shown in Table I. The dynamics of the biped are computed in the MATLAB/Simulink environment. The dynamics parameters are expressed in C language code by using “c-code” command for faster computation and simulation. The control algorithms are simulated in Microsoft VC++ environment using the C code of the biped dynamics generated by MATLAB/Simulink.

TABLE II
BIPED'S JUMPING GAIT

Phase	θ_j^d	$a_{j,0}$	$a_{j,1}$	$a_{j,2}$	$a_{j,3}$	$a_{j,4}$
Take-off	2	2.362	0.5441	-41.51	351.0	-1707.0
	3	-1.519	-1.052	79.32	-677.7	3313.0
	4	1.527	-4.826	-37.8	326.7	-1606.0
Flight	2	1.589	2.251	49.69	-537.9	1178.0
	3	-0.03766	-4.733	-105.8	1144.0	-2506.0
	4	0.5023	3.247	32.36	-423.3	922.9
Touch-down	2	2.3638	0	0	0	0
	3	-1.5217	0	0	0	0
	4	1.5286	0	0	0	0

The integration algorithm is based on the fourth-order Runge-Kutta method with a fixed step size of 0.0001 s.

The initial posture of the biped considered is $\theta_a = [0 \ 2.3638 \ -1.5217 \ 1.5286]^T$ rad with zero joint angular velocities. With the initial posture, the location of CM is $x_{CM}(0) = 0.0646$ m and $y_{CM}(0) = 0.1155$ m. It is noticeable that $0 < x_{CM}(0) < d_1$, which indicates that the biped starts from a statically stable posture. The toe-ground contact point is considered as mentioned in C2), and the parameters for the ankle-ground contact points are as follows⁸: $K_4 = 40000$ N·m and $K_5 = 800$ s⁻¹. The values of K_4 and K_5 used in the simulation are adjusted such that the negative value of θ_1 is within -0.001 rad in subsystem B, and there is no rebound at the ankle-ground contact points. The negative value of θ_1 corresponds to the penetration into the ground at the ankle-ground contact points. Since θ_1 is within -0.001 rad in subsystem B, the penetration is approximately 0.1 mm in simulation. The desired polynomial coefficients of the shape variables $\theta_j^d(t)$ are chosen based on the method described in Section IV and are shown in Table II. The values of different quantities during jumping are shown in Table III.

In takeoff phase of the jumping gait, the takeoff time is 0.15 s, $C_x = 0$, and $C_y = 0.55$ m/s. The control law (20) with feedback gains $K_p = 60$ and $K_d = 80$ is applied in the takeoff phase. The final CM velocities are $\dot{x}_{CM}(0) = 0.2275$ m/s and $\dot{y}_{CM}(0) = 0.5143$ m/s. These act as initial conditions for the flight phase.

In flight phase of the jumping gait, $t_f = 0.15$ s, $\eta^d = 0.025$ m, and $\zeta^d = 0$. In the flight phase, the control input is as in (20) with feedback gains $K_p = 400$ and $K_d = 300$. Impact occurs at the end of the flight phase. Joint angular velocities change instantaneously according to (15), which leads to change in angular momentum according to (17). Due to impulsive-dynamical assumption on the impact, the joint angular positions are constant during the impact interval. Joint angular positions and velocities after the impact act as initial conditions for the touchdown phase. After the impact, $\sigma(0) = -1.62$ kg·m²·s⁻¹, and $\theta_1(0) = 0.1063$ rad. The flight time is 0.1366 s in simulation (see Table III).

The actual height (η) and length (ζ) of jumping are computed by

$$\begin{bmatrix} \zeta \\ \eta \end{bmatrix} = \begin{bmatrix} 0 & 0 & 0 & 0 & 1 & 0 \\ 0 & 0 & 0 & 0 & 0 & 1 \end{bmatrix} \theta_f - f_{CM}(\theta_a). \quad (40)$$

⁸ K_4 and K_5 are chosen according to the range reported in [33].

The flight phase is indicated by $\eta > 0$. $\zeta < 0$ indicates that the biped is jumping forward, while $\zeta > 0$ indicates that the biped is jumping backward. With the parameters in Table II, the biped jumped backward 7 mm, and the maximum jumping height is 0.0249 m in simulation (see Fig. 10).

The desired gait in the touchdown phase is the same as the initial posture of the biped. In the touchdown phase, the control law (20) with feedback gains $K_P = 9$, $K_D = 6$, and $\epsilon = 0.1$ is applied.

Table III shows the values of the various parameters during the jumping phases obtained in simulation (joint angular positions, velocities, and torque inputs are discussed in Section VI-B). The touchdown phase is run in simulation for 5 s. Joint angular positions converge to the initial positions with time in the touchdown phase. Angular velocities converge to zero with time in the touchdown phase (after 2.0 s). Fig. 11 shows the variation of τ_1 in the touchdown phase. Due to sudden change in angular velocities at point of impact, $\tau_1 = 37.3042$ N·m.

1) *Stability in Touchdown Phase:* With the control input (20) and the desired gaits as per Table II, the values of different joint angles and velocities are shown in Table III. Considering the final posture as $\theta_a = [0 \ 2.3638 \ -1.5217 \ 1.5286]^T$ rad with zero joint angular velocities, $K_1 = 27.6501$ kg⁻¹·m⁻², $K_2 = 1.6873$ N·m, and $K_3 = 0.5101$ rad. The corresponding stable equilibrium point of ZD (31) is $(-0.000021, 0)$. The stability conditions CLD1-CLD3 converge to SZD1-SZD3 when the *internal dynamics* in (36) converge to SZD (31). Therefore, the stability of the CLD (CLD1-CLD3) also implies the stability of the SZD (SZD1-SZD3).

The stability in the touchdown phase is verified by CLD1-CLD3. Angular positions and velocities in Table III at $t = 0.2867$ s indicate $\sigma(0) = -0.1620$ kg·m²·s⁻¹ and $\theta_1(0) = 0.1063$ rad. Table IV shows the $V_{x_{CM}}^{\max}$ and V_{ID}^{\max} values. It can be verified that CLD1 and CLD2 are satisfied. Fig. 12 shows the plots for θ_1 versus σ and κ_3 versus σ with $K_4 = 40000$ N·m, $K_5 = 800$ s⁻¹, and $\epsilon = 0.1$. It is seen that all the time, $\theta_1 < \kappa_3$, i.e., $x_{CM}(\theta_a) > 0$. CLD3 is satisfied as θ_1 converges to the stable equilibrium point $(-0.000021, 0)$ with time. The conditions CLD1-CLD3, for the stability of the touchdown phase CLD, are satisfied.

B. Jumping Experiment With the BRAIL 2.0 Biped

For jumping gait realization, actuators (see Section II-A1) are operated in torque control mode ("endless turn mode"). The input torques to the actuators are computed based on the control law (20). The control law (20) computes torques inputs at ankle, knee, and hip. The ankle, knee, and hip joints have two actuators each, with one placed at each leg. The actuator inputs are half of the joint torques computed by the control law (20).

The control law (20) uses the bipedal dynamics, and computation of bipedal dynamics needs the joint angular position and velocity feedback. The controller (see Section II-A2) reads the feedback from the actuators and computes the biped dynamics at each sampling instant. Controller sampling time is 0.01 s, i.e., controller applies the control input (20) to each actuators for 0.01 s. The controller gains are chosen as described in

TABLE III
DIFFERENT PARAMETERS VALUES AT JUMPING PHASES

Phase	Time (Seconds)	θ_1 (rad)	θ_2 (rad)	θ_3 (rad)	θ_4 (rad)	$\dot{\theta}_1$ (rad/s)	$\dot{\theta}_2$ (rad/s)	$\dot{\theta}_3$ (rad/s)	$\dot{\theta}_4$ (rad/s)	$x_{cm}(\theta_a)$ (m)	$y_{cm}(\theta_a)$ (m)
Take-off	0	0	2.3638	-1.5217	1.5286	0	0	0	0	0.0646	0.1155
	0.15	0.2646	1.8314	-0.5049	0.2492	0.9529	-11.2516	21.6933	-15.7940	0.0600	0.1797
Flight	0.1501	0.2646	1.8314	-0.5049	0.2492	0.9529	-11.2516	21.6933	-15.7940	0.0600	0.1797
	0.2866	0.1063	2.0276	-0.9337	0.5272	-1.9108	-2.4983	5.2413	-1.8405	0.0841	0.1585
Impact	0.2866	0.1063	2.0276	-0.9337	0.5272	-9.7475	5.0864	9.1061	-6.4239	0.0841	0.1585
Touch-down	0.2867	0.1063	2.0276	-0.9337	0.5272	-9.7475	5.0864	9.1061	-6.4239	0.0841	0.1585
	5.2867	0	2.3638	-1.5217	1.5286	0	0	0	0	0.0646	0.1155

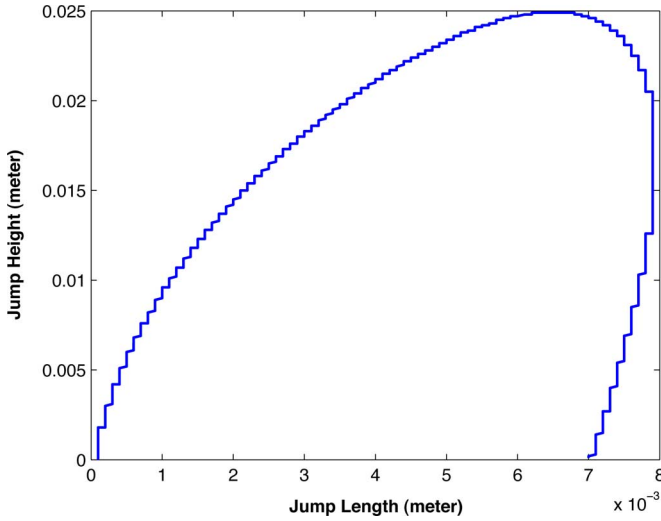


Fig. 10. Jumping height (ζ) versus jumping length (η).

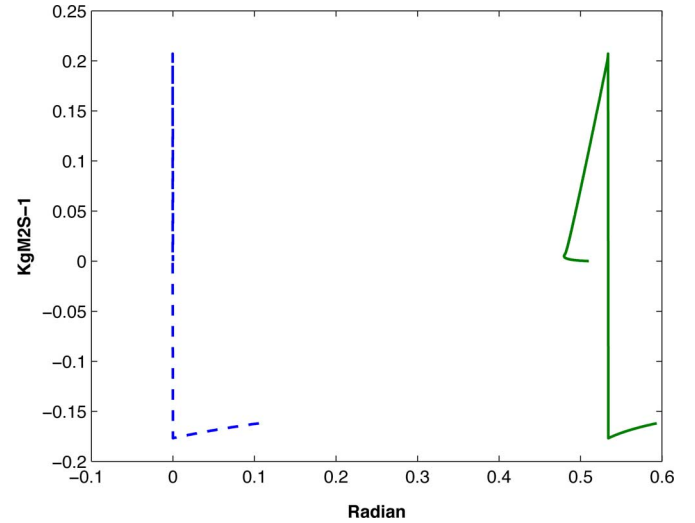


Fig. 12. θ_1 versus σ (dotted) and κ_3 versus σ (solid).

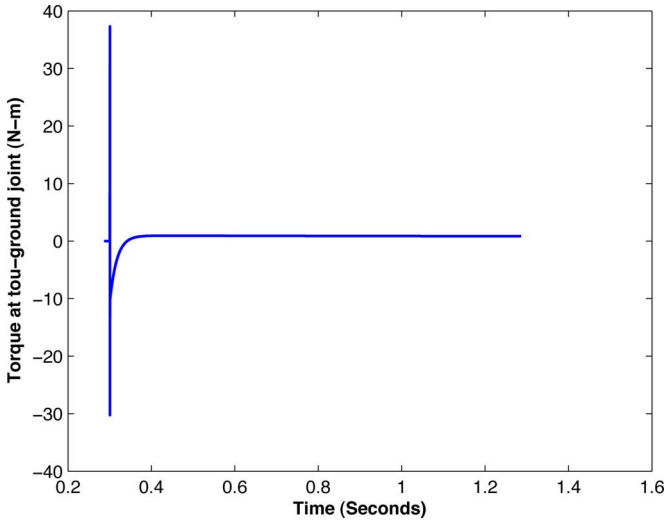


Fig. 11. τ_1 at touchdown phase.

simulation. The control inputs change according to the change in desired joint angular positions from $\theta_{bs}^d(t)$ to $\theta_{bf}^d(t)$ at $t = 0.15$ s and $\theta_{bf}^d(t)$ to $\theta_{bl}^d(t)$ at $t = 0.33$ s. The torque inputs are read from the actuator “load” feedback at each sampling instant and are plotted in Fig. 13. The torque readings are collected from joint actuators (ankle, knee, and hip) both from the right and left legs at each sampling instant. Fig. 13(a)–(c) shows the experimental

result as the sum of the “load” readings of both the joint actuators placed at the ankle, knee, and hip of each leg, respectively.

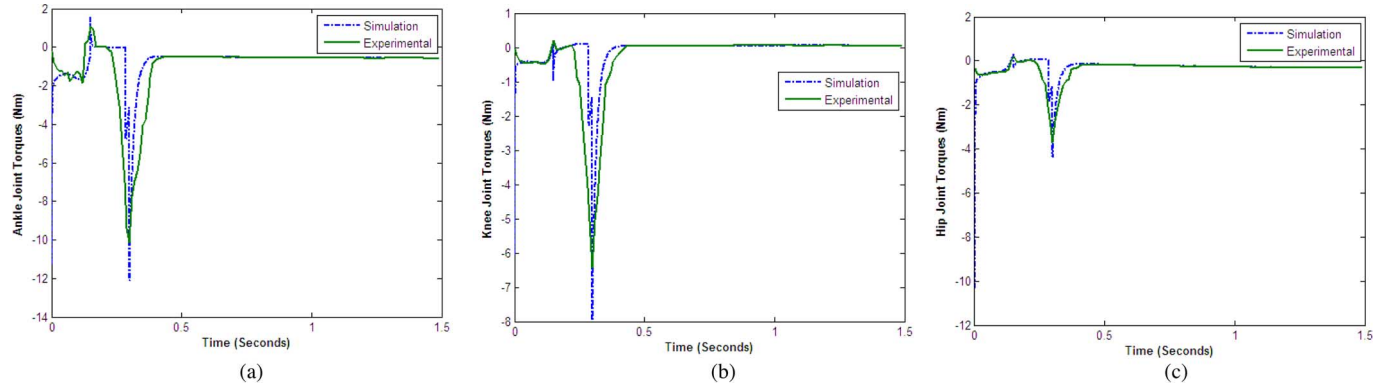
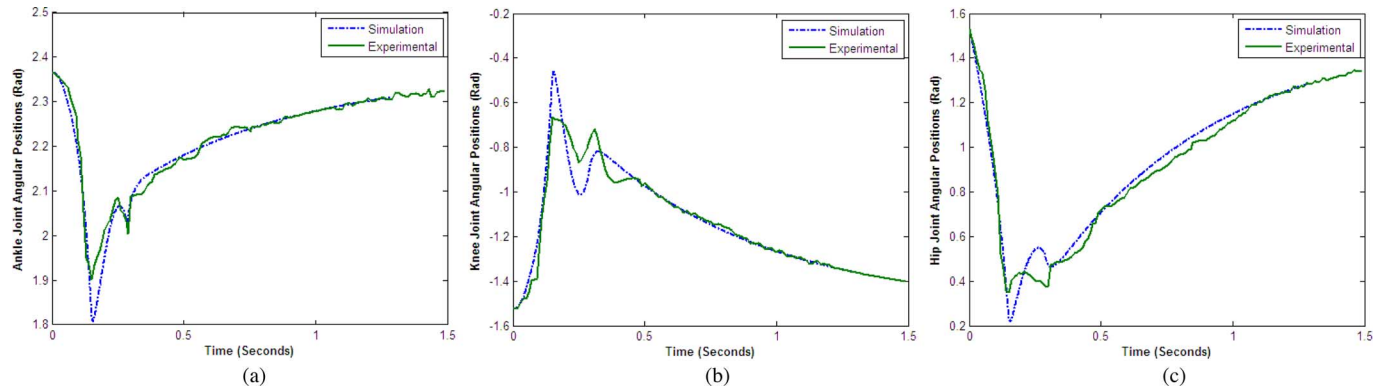
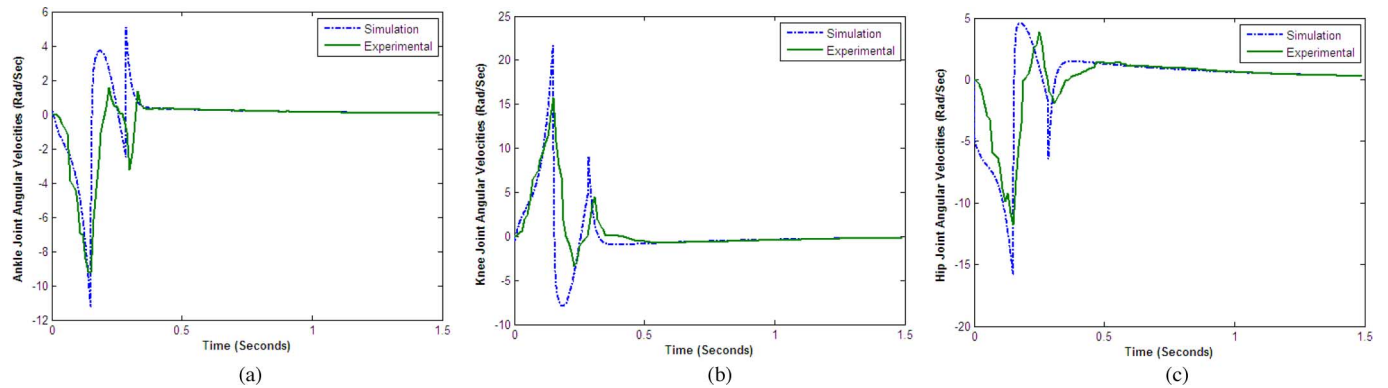
Figs. 14 and 15 show the variation of joint angular positions and velocities with control inputs according to (20) for the first 1.5 s during jumping. Joint angular position and velocity feedback are read from both the right and left legs. As the readings from both the actuators placed at the ankle, knee, and hip joints of the legs are almost equal, Figs. 14 and 15 show the readings from the left leg actuators.

The biped’s absolute orientation at $t = 0.15$ s (at the end of takeoff phase) is $\theta_a = [0.19 \ 1.90 \ -0.66 \ 0.35]^T$ rad. The joint angular velocities $\dot{\theta}_a = [0.85 \ -9.25 \ 15.69 \ -11.77]^T$ rad/s at $t = 0.15$ s. θ_1 and $\dot{\theta}_1$ are computed from the internal dynamics (36) (by fourth-order Runge–Kutta method with a fixed step size of 0.01 s) using the measured actuator positions and velocities. The desired joint angular positions change from $\theta_{bs}^d(t)$ to $\theta_{bf}^d(t)$ at $t = 0.15$ s (takeoff phase to flight phase).

In the flight phase, the joint angular positions and velocities (experimental and simulation) between $t = 0.15$ and $t = 0.29$ s are shown in Figs. 14 and 15. The biped’s absolute orientation and joint angular velocities at $t = 0.30$ s (at the end of the flight phase) are $\theta_a = [0.08 \ 2.09 \ -0.74 \ 0.38]^T$ rad and $\dot{\theta}_a = [-0.76 \ -3.23 \ 3.57 \ -1.38]^T$ rad/s. Impact takes place during $t = 0.30$ – 0.33 s (sensed by the sudden change in joint velocities). The impact model in Section II-F assumes nonelasticity, i.e., instantaneous change in velocity at the point of impact. However, it is noted from the Fig. 15 that velocities change fast

TABLE IV
 $V_{x_{CM}}^{\max}$ AND V_{ID}^{\max}

		$\theta_1(0)$ (rad)	θ_2 (rad)	θ_3 (rad)	θ_4 (rad)	$\dot{\theta}_1$ (rad/s)	$\dot{\theta}_2$ (rad/s)	$\dot{\theta}_3$ (rad/s)	$\dot{\theta}_4$ (rad/s)	$x_{cm}(\theta_a)$ (m)	$\sigma(0)$ kgm^2s^{-1}
$V_{x_{cm}}^{\max}$ (m^2)	0.00	0.5934	2.0276	-0.9337	0.5272	-9.7475	5.0864	9.1061	-6.4239	0.000	-0.1619
V_{ID}^{\max} ($kg^2m^4s^{-2}$)	0.015	0.1063	2.0276	-0.9337	0.5272	-4.3864	5.0864	9.1061	-6.4239	0.0841	0.1732

Fig. 13. Variations of the joint torques in experimental and simulation studies. (a) τ_2 . (b) τ_3 . (c) τ_4 .Fig. 14. Variation of the joint angular positions in experimental and simulation studies. (a) θ_2 . (b) θ_3 . (c) θ_4 .Fig. 15. Variation of the joint angular velocities in experimental and simulation studies. (a) $\dot{\theta}_2$. (b) $\dot{\theta}_3$. (c) $\dot{\theta}_4$.

during the impact (from 0.30 to 0.33 s) but not instantaneously. The joint velocities keep changing fast from 0.01 to 0.03 s after the feet touch the ground. Such an effect is more prominent in ankle joint velocity as it changes from negative to positive during the impact (see Table III). The joint positions and velocities

become $\theta_a = [0.0451 \ 2.0919 \ -0.7259 \ 0.3629]^T$ rad and $\dot{\theta}_a = [-5.44 \ 1.34 \ 4.50 \ -1.90]^T$ rad/s at $t = 0.33$ s after the impact.

After the impact, $\sigma(0) = -0.1362 \text{ kg}\cdot\text{m}^2\cdot\text{s}^{-1}$ and $\theta_1(0) = 0.0451$ rad. The control inputs change at $t = 0.33$ s, as desired

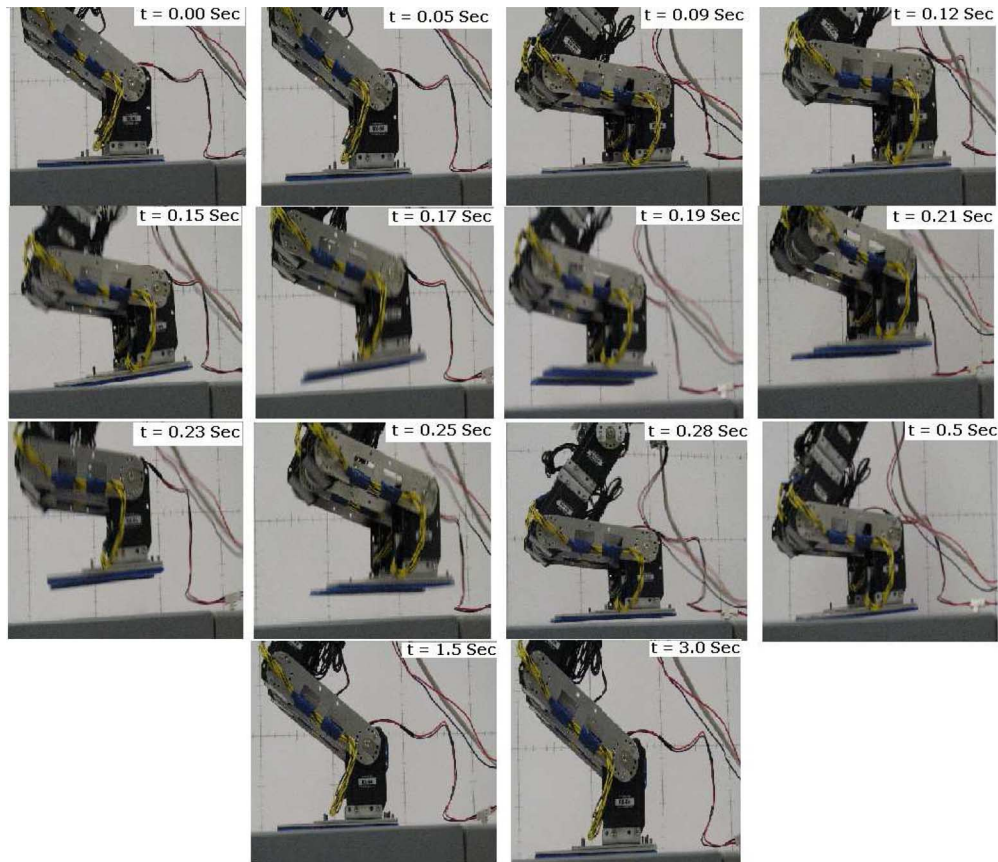


Fig. 16. Jump sequence with control input (20) and desired gait as per Table II.

joint angular positions change from $\theta_{bf}^d(t)$ to $\theta_{bl}^d(t)$ at $t = 0.33$ s (after the impact). With the control input (20) and the feedback gains, $K_P = 9$, $K_D = 6$, $\epsilon = 0.1$, $V_{x_{CM}}^{\max} = 0$, and $V_{ID}^{\max} = 0.0115 \text{ kg}^2 \cdot \text{m}^4 \cdot \text{s}^{-2}$. The stability conditions CLD1 and CLD2 are satisfied, which results in the stability of subsystem A. The biped's angular positions and velocities in the touchdown phase converge to $\theta_{bl}^d(t)$ and $\dot{\theta}_{bl}^d(t)$ with stable landing.

With the desired gaits as per Table II and the control input as per (20), the biped's jumping sequence is shown in Fig. 16. The maximum jumping height measured is ~ 0.025 m. The biped could jump backward by 0.004 m.

C. Comments on Simulations and Experimental Results

In Figs 13–15, certain deviations of the actual input torques, joint positions, and velocities from the simulation results are noted. Following are the possible causes of such deviations.

- 1) *Actuator time constant*: Considering the controller's sampling time of 0.01 s, the actuator time constant (0.002–0.006 s depending on the load) essentially introduces both actuation and measurement latency.
- 2) *Impact model*: The nonelasticity assumption on the impact model in Section II-F is not completely satisfied.
- 3) *Foot-ground contact model*: The estimated ranges of K_4 and K_5 might not be able to exactly model the behavior of the foot-ground contact surface. Moreover, jumping performance varies, depending on the nature of the ground

surface such as wood or cement. The experimentations in Section VI-B are performed on a cement surface.

- 4) *Sampling time*: The experimental results sometimes fail to capture certain features (i.e., exact peak values) of the simulated plots (with an integration step size of 0.0001 s) due to larger sampling time (0.01 s).
- 5) *Mismatches in dynamic parameters*: The estimated biped parameters in Table I (using *Autodesk* and *Msc. Visualnastran*) might not be exact.

However, the actual input torques, joint positions, and velocities could capture the key aspects related to the stability analysis discussed in Section V. The biped's jumping performance, with stable landing, is quite close to the simulated results (jumping height is almost the same as in simulation), even in the presence of the mismatches between simulation and experimental environments. The following points are notable on the robustness of the controller.

- 1) From the experimental data shown in Fig. 13, it is noted that the actual control inputs do not exactly match the simulated inputs. The biped could jump stably in spite of the difference between simulated and actual control inputs.
- 2) Robustness in the controller can be quantified by the conditions CLD1 and CLD2. The controller parameters, i.e., K_P , K_D , and ϵ , can be chosen such that there is more of a stability margin. As long as CLD1–CLD3 are satisfied, the landing is stable, even in the presence of disturbances.

VII. CONCLUSION

A rigorous stability analysis has been carried out for a planar, four-link biped model to achieve jumping gaits with stable landing on a flat surface (i.e., ground). The foot compliance is modeled as a spring–damper system at the ankle and as a rigid pivot at the toe. In the landing (touchdown) phase, the foot link can either rotate about the toe or remain flat on the ground surface. The foot rotation introduces an additional passive DOF at the joint between the toe and the ground that further results in 2-D ZD manifold due to underactuation. During landing (in the touchdown phase), switching occurs between the biped configurations with foot rotation (see subsystem A in Fig 8) and with a flat foot (see subsystem B in Fig 8). Because of such switchings, the system’s ZD during landing phase is termed as “SZD.” The stability of SZD and its relation with the stability of CLD are addressed to investigate landing stability.

The local asymptotic stability of the SZD is established using the multiple Lyapunov function (MLF) approach. The stability of SZD depends on the biped configuration (K_1 , K_2 , and K_3), landing posture and the joint velocities (θ_{10} and σ_0), and the nature of the surface (K_4 and K_5). However, the local stability of SZD does not essentially guarantee the stability of CLD. The stability of CLD further depends on the *critical potential index* and *critical kinetic index*. The values of *critical potential index* and *critical kinetic index* reflect the restrictions on the initial landing posture and the joint velocities of the biped [$\xi_1(0)$, $\xi_2(0)$, $\theta_1(0)$, and $\sigma(0)$], as well as on the control parameters (K_P , K_D , and ϵ), which are necessary for stable landing. Singular perturbation approach is used to investigate the stability of CLD and its dependence on the perturbation parameter ϵ . With $\epsilon = 0$, the CLD converges to SZD and the conditions CLD1–CLD3 (Theorem 4) converge to the conditions SZD1–SZD3 (Theorem 3). The stability of CLD (stable landing) requires the stability of SZD and certain additional restrictions based on the values of *critical potential index* and *critical kinetic index*.

The jumping gait is realized on BRAIL 2.0 biped. The stability studies are validated by the experimental results. The choice of various jumping parameters is dependent on the dynamics of the biped. The validity of the jumping parameters is verified offline. Therefore, the jumping gaits are computed offline and implemented on the BRAIL 2.0 biped. The jumping performance is restricted by the maximum torque provided by the actuator.

A. Future Directions

The reported research has two notable extensions/improvements.

- 1) Due to space limitations, the analysis in this research is confined to the situation when the biped lands on its toe. However, the analysis can further be extended for the situation when the biped lands on its heel. Combining the two situations, it is possible to propose a certain ground reference point, the location of which indicates generic stability properties during landing (on either the heel or toe). Such ground reference points can be useful for stability analysis of biped locomotion.

- 2) The selection of desired jumping gaits (see Section IV) involves the proper choice of a number of parameters, i.e., C_x , C_y , η^d , ζ^d , and the various controller gains. In this research, the selection of desired jumping gaits does not involve system dynamics. However, it would be an interesting direction to include dynamics in the selection process of desired gait parameters. It would be a multiobjective optimization problem to choose such parameters to meet a desired jumping performance, i.e., jumping height and length, and effect of impact.

APPENDIX I

PROOF OF THEOREM 1

Proof: From (33), for subsystem A

$$\begin{aligned} \frac{d\sigma}{d\theta_1} &= \frac{K_2 \sin(\theta_1 - K_3)}{K_1 \sigma} \\ \sigma d\sigma &= \frac{K_2}{K_1} \sin(\theta_1 - K_3) d\theta_1 \\ \frac{\sigma_0^2}{2} &= \frac{\sigma^2}{2} + V_{ZD}(\theta_1) \\ \sigma_0^2 &= \sigma^2 + 2V_{ZD}(\theta_1) \end{aligned} \quad (41)$$

where $V_{ZD}(\theta_1)$ is defined as follows:

$$\begin{aligned} V_{ZD}(\theta_1) &= - \int_{\theta_{10}}^{\theta_1} \frac{K_2}{K_1} \sin(\theta_1 - K_3) d\theta_1 \\ &= \frac{K_2}{K_1} (\cos(\theta_1 - K_3) - \cos(\theta_{10} - K_3)). \end{aligned} \quad (42)$$

The maximum value of $V_{ZD}(\theta_1)$ in (42) occurs when $\theta_1 = K_3$. The corresponding maximum value is denoted by V_{ZD}^{\max} , which is calculated by putting $\theta_1 = K_3$ in (42)

$$V_{ZD}^{\max} = \frac{K_2}{K_1} (1 - \cos(\theta_{10} - K_3)). \quad (43)$$

Equation (41) shows that if $|\sigma_0| > \sqrt{2V_{ZD}^{\max}}$, $\sigma = 0$ does not exist in the σ trajectory because $|\sigma_0| \not\geq \sqrt{2V_{ZD}^{\max}}$ at $\sigma = 0$. Similarly, $|\sigma_0| < \sqrt{2V_{ZD}^{\max}}$ indicates the existence of $\sigma = 0$, i.e., zero-crossing in the σ trajectory. Fig. 8 shows the vector field of the SZD. Depending on the initial state, there can be four cases for $\theta_{10} > 0$.

- 1) With $K_3 > \theta_{10}$ and $\sigma_0 > 0$, the trajectories in subsystem A (33) reach the $\theta_1 = 0$ plane if there exists a zero-crossing in the σ trajectory. The zero-crossing exists when $|\sigma_0| < \sqrt{2V_{ZD}^{\max}}$, i.e., $\sigma_0 < \sqrt{2V_{ZD}^{\max}}$ for $\sigma_0 > 0$.
- 2) With $K_3 > \theta_{10}$ and $\sigma_0 < 0$, the trajectories in subsystem A (33) always reach the $\theta_1 = 0$ plane.
- 3) With $K_3 \leq \theta_{10}$ and $\sigma_0 > 0$, the trajectories in subsystem A (33) never reach the $\theta_1 = 0$ plane.
- 4) With $K_3 \leq \theta_{10}$ and $\sigma_0 < 0$, the trajectories in subsystem A (33) reach the $\theta_1 = 0$ plane if there is no zero-crossing in the σ trajectory. Zero-crossing exists if $|\sigma_0| > \sqrt{2V_{ZD}^{\max}}$, i.e., $\sigma_0 < -\sqrt{2V_{ZD}^{\max}}$ for $\sigma_0 < 0$.

Cases 1) and 2) prove part 1), while cases 3 and 4 prove part 2) of Theorem 1.

It can be noted that (33) represents the dynamics of a double-inverted pendulum or acrobat [9], [27]. The conditions in Theorem 1 ensure that the initial conditions do not correspond to the separatrix passing through the equilibrium point $(K_3, 0)$. ■

APPENDIX II

PROOF OF THEOREM 2

Proof: Assume the solution vector of (33) reaches the $\theta_1 = 0$ plane at $(0, \sigma_T)$. From the ZD (34)

$$\begin{aligned} \frac{d\sigma}{d\theta_1} &= \frac{K_2 \sin(\theta_1 - K_3) - K_4\theta_1 - K_5\sigma}{K_1\sigma} \\ \int_{\sigma_T}^{\sigma} \sigma d\sigma &= \int_0^{\theta_1} \frac{K_2 \sin(\theta_1 - K_3) - K_4\theta_1 - K_5\sigma}{K_1} d\theta_1 \\ \frac{\sigma_T^2}{2} &= V_B(\theta_1, \sigma) + K_5 \int_B \sigma^2 dt \end{aligned} \quad (44)$$

where $V_B(\theta_1, \sigma)$ is given by

$$V_B(\theta_1, \sigma) = -\int_0^{\theta_1} \frac{K_2 \sin(\theta_1 - K_3) - K_4\theta_1}{K_1} d\theta_1 + \frac{\sigma^2}{2}. \quad (45)$$

Equation (44) shows that $V_B(\theta_1, \sigma) > 0$ for $K_5 < \sigma_T^2/2 \int_B \sigma^2 dt$ and $\dot{V}_B(\theta_1, \sigma) = -K_5\sigma^2$. Hence, $V_B(\theta_1, \sigma)$ is positive-definite, and its time derivative $\dot{V}_B(\theta_1, \sigma)$, along the ZD (34), is negative semidefinite when $0 < K_5 < \sigma_T^2/2 \int_B \sigma^2 dt$. $\dot{V}_B(\theta_1, \sigma) = 0$ if $\sigma = 0$, which leads to $K_2 \sin(\theta_1 - K_3) - K_4\theta_1 = 0$, the solution of which is the equilibrium point $(-(K_2 \sin(K_3)/K_4), 0)$. Therefore, $V_B(\theta_1, \sigma)$ is a *candidate Lyapunov function* [10] for $0 < K_5 < \sigma_T^2/2 \int_B \sigma^2 dt$, and local asymptotic stability of the equilibrium point $(-(K_2 \sin(K_3)/K_4), 0)$ is proved using *LaShelle's invariance principle* [28]. ■

The following are noticeable in subsystem B.

- 1) As $\dot{V}_B(\theta_1, \sigma) = -K_5\sigma^2$, convergence to equilibrium is faster when K_5 is higher. With higher K_5 (but less than $\sigma_T^2/2 \int_B \sigma^2 dt$), the chances of rebounding at the ankle-ground contact points are less.
- 2) For the trajectory σ_T to σ_F (see Fig. 8), $\int_{\sigma_T \rightarrow \sigma_F} [(K_2 \sin(\theta_1 - K_3) - K_4\theta_1)/K_1] d\theta_1 = 0$. Therefore

$$\sigma_F^2 = \sigma_T^2 - 2K_5 \int \sigma^2 dt. \quad (46)$$

In the case of bouncing back from the ankle-ground contact points, let the trajectories intersect with the $\theta_1 = 0$ plane at $\tilde{\sigma}_F$ (for $\sigma > 0$) and $\tilde{\sigma}_T$ (for $\sigma < 0$) (see Fig. 8). Equation (46) is true for the trajectories $\tilde{\sigma}_T$ to $\tilde{\sigma}_F$.

APPENDIX III

PROOF OF THEOREM 3

Proof: SZD1 and SZD2 are sufficient to ensure (33) to reach the $\theta_1 = 0$ plane (from Theorem 1). SZD3 is sufficient to ensure local asymptotic stability of (34) (from Theorem 2). The stability of the SZD (31) is analyzed using the MLF approach [31].

The MLF approach is based on the existence of the *Lyapunov-like* functions for every subsystem within the switching system. The existence of *Lyapunov-like* functions for every subsystem in a switching system indicates the Lyapunov stability of the switching system. The *Lyapunov-like* function is defined as *candidate Lyapunov function* with at least negative semidefinite first derivative and monotonically nonincreasing values at the switching plane during switching in a specific direction [31]. Let us define $V_A(\theta_1, \sigma)$ as

$$V_A(\theta_1, \sigma) = \frac{\sigma^2}{2} + V_{ZD}(\theta_1). \quad (47)$$

Equation (41) shows that $V_A(\theta_1, \sigma) > 0$ for $\sigma_0 \neq 0$ and $\dot{V}_A(\theta_1, \sigma) = 0$. Therefore, $V_A(\theta_1, \sigma)$ is a *candidate Lyapunov function* for subsystem A. Similarly, $V_B(\theta_1, \sigma)$ (45) is a *candidate Lyapunov function* for subsystem B. Therefore, V_A and V_B are positive-definite, and their first derivatives are at least negative semidefinite. The monotonicity of V_A and V_B can be shown considering the first few switchings. Suppose the first switching occurs at $(0, \sigma_T)$ from subsystem A to subsystem B, the second switching occurs at $(0, \sigma_F)$ from subsystem B to subsystem A, the third switching occurs at $(0, \tilde{\sigma}_T)$ from subsystem A to subsystem B, and the fourth switching occurs at $(0, \tilde{\sigma}_F)$ from subsystem B to subsystem A (see Fig. 8). Equation (41) leads to (46) indicating $|\sigma_F| < |\sigma_T|$ and (41) leads to $|\tilde{\sigma}_T| = |\sigma_F|$. As a result, $\sigma_T > \tilde{\sigma}_T$, $\sigma_F > \tilde{\sigma}_F$, $V_B(0, \sigma_T) > V_B(0, \tilde{\sigma}_T)$, and $V_A(0, \sigma_F) > V_A(0, \tilde{\sigma}_F)$. Therefore, V_A and V_B are monotonically decreasing (nonincreasing) at the switching plane in any particular direction of switching. Hence, V_A and V_B are *Lyapunov-like* functions for subsystems A and B, respectively. This proves the local asymptotic stability of the SZD.

It is noticeable that the stability of SZD requires $|\sigma_0| < \sqrt{(2K_2/K_1)(1 - \cos(\theta_{10} - K_3))}$, i.e., SZD2 (does not allow $\sigma_0 < -\sqrt{(2K_2/K_1)(1 - \cos(\theta_{10} - K_3))}$), which is not true in ZD1 for subsystem A. Basically, SZD2 ensures the monotonic property of the candidate Lyapunov functions V_A and V_B . ■

APPENDIX IV

PROOF OF THEOREM 4

Proof: Singular perturbation approach is used to prove the stability of the internal dynamics (36) [10], [28]. As the perturbation parameter ϵ in (36) changes, the system splits into two time-scaled dynamics [28]. With $\epsilon = 0$ in (36), the dynamics indicate the “slow dynamics.” System dynamics with small positive nonzero ϵ indicate the “quasi-steady-state” dynamics [28]. For the stability of the overall system, both the “slow dynamics” and the “quasi-steady-state” dynamics must be stable.

The first two equations of (36) can be rewritten as (48). In (48), with $\epsilon \rightarrow 0$, $\xi_1 \rightarrow 0$ and $\xi_2 \rightarrow 0$, which leads to $\theta_b \rightarrow \theta_{bl}^d$ and $\dot{\theta}_b \rightarrow 0$. This further leads to $\kappa_1(\xi_1) \rightarrow K_1$, $\kappa_2(\xi_1) \rightarrow K_2$, and $\kappa_3(\xi_1) \rightarrow K_3$. Therefore, for $\epsilon = 0$, the *internal dynamics* (36) converge to SZD (31). The SZD (31) is locally asymptotically stable in a neighborhood specified by the conditions SZD1–SZD3. For $\epsilon = 0$, (36) becomes locally asymptotically stable in a neighborhood specified by SZD1–SZD3 [32]. Hence, the “slow dynamics” with $\epsilon = 0$ are locally asymptotically stable in

a neighborhood specified by SZD1–SZD3

$$\begin{aligned}\dot{\xi}_1 &= \xi_2 \\ \epsilon^2 \dot{\xi}_2 &= -K_P \xi_1 - \epsilon K_D \xi_2.\end{aligned}\quad (48)$$

If $\epsilon \neq 0$ is a small positive number, then (36) reflects the “quasi-steady-state” behavior. In (39), $|x_{CM}(\theta_{a0})| < \sqrt{2V_{x_{CM}}^{\max}}$ indicates the existence of zero-crossing in the $x_{CM}(\theta_a)$ trajectory. Similarly, $|\sigma(0)| < \sqrt{2V_{\sigma}^{\max}}$ in (38) indicates the existence of zero-crossing in the σ trajectory. If $x_{CM}(\theta_{a0}) > 0$, $\kappa_3(\xi_1) > \theta_1$ (see Lemma 1). As per CLD1, $x_{CM}(\theta_a)$ never changes sign and does not have zero-crossing, which leads to $\kappa_3(\xi_1) > \theta_1$. As per CLD2, a zero-crossing exists in the σ trajectory. Hence, CLD1 and CLD2 ensure that the system (36) follows trajectory I to reach the $\theta_1 = 0$ plane (see Fig. 9).

In subsystem B, with $\epsilon \neq 0$, the equilibrium point is computed by equating the last two equations of (36) to zero for $\xi_1 \neq 0$ and $\xi_2 \neq 0$. Considering $(\xi_1, \xi_2, \theta_1^e, \sigma^e)$ as the equilibrium of (36) with $\epsilon \neq 0$, θ_1^e and σ^e are given by⁹

$$\begin{aligned}\theta_1^e &\approx -\frac{\kappa_2(\xi_1) \sin(\kappa_3(\xi_1)) + K_5(\kappa_4(\xi_1)\xi_2/\kappa_1(\xi_1))}{K_4} \\ \sigma^e &= \frac{\kappa_4(\xi_1)\xi_2}{\kappa_1(\xi_1)}.\end{aligned}\quad (49)$$

To analyze the stability of the equilibrium point $(\xi_1, \xi_2, \theta_1^e, \sigma^e)$, the candidate Lyapunov function V_B^ϵ is chosen as (50). With $\sigma_T^2/2 \int_B \sigma^2 dt > K_5 > 0$ as mentioned in CLD3, V_B^ϵ is positive-definite

$$V_B^\epsilon = \frac{\sigma_T^2}{2} - K_5 \int_B \sigma^2 dt + \left(\frac{K_P}{\epsilon^2} \xi_1^2 + \xi_2^2 \right) \frac{1}{2}.\quad (50)$$

The time derivative of V_B^ϵ , which is computed along system dynamics, is given by

$$\begin{aligned}\dot{V}_B^\epsilon &= -K_5 \sigma^2 + \left(\frac{K_P}{\epsilon^2} \xi_1 \dot{\xi}_1 + \xi_2 \dot{\xi}_2 \right) \\ &= -K_5 \sigma^2 + \frac{K_P}{\epsilon^2} \xi_1 \xi_2 + \xi_2 \left(-\frac{K_P}{\epsilon^2} \xi_1 - \frac{K_D}{\epsilon} \xi_2 \right) \\ &= -K_5 \sigma^2 - \frac{K_D}{\epsilon} \xi_2^2.\end{aligned}\quad (51)$$

$\dot{V}_B^\epsilon = 0$ when $\sigma = 0$ and $\xi_2 = 0$, which further leads to $\xi_1 = 0$. In this case, with $\xi_1 = 0$ and $\xi_2 = 0$, the system will behave like SZD (31), which is locally asymptotically stable. Hence, $\dot{V}_B^\epsilon < 0$ if CLD3 is true. The local asymptotic stability in subsystem B is achieved by CLD3. CLD1–CLD3 ensure the stability of the “quasi-steady-state” system.

The “slow dynamics” correspond to SZD and are locally asymptotically stable if SZD1–SZD3 are true. The “quasi-steady-state” system is asymptotically stable if CLD1–CLD3 are true. CLD1–CLD3 converge to SZD1 and SZD2 with time. Hence, the switching system (36) is locally asymptotically stable if CLD1–CLD3 are true. ■

⁹ θ_1^e is small compared with $\kappa_3(\xi_1)$ in subsystem B, i.e., $\sin(\theta_1 - \kappa_3(\xi_1)) \approx -\sin(\kappa_3(\xi_1))$.

REFERENCES

- [1] M. Vukobratović, *Biped Locomotion: Dynamics, Stability, Control and Application*. New York: Springer-Verlag, 1990.
- [2] K. Nagasaka, Y. Kuroki, S. Suzuki, Y. Itoh, and J. Yamaguchi, “Integrated motion control for walking, jumping and running on a small bipedal entertainment robot,” in *Proc. IEEE Int. Conf. Robot. Autom.*, Apr. 26–May 1, 2004, vol. 4, pp. 3189–3194.
- [3] P. Vadakkepat, D. Goswami, and C. M. Hwee, “Disturbance rejection by online ZMP compensation,” *Robotica*, vol. 26, pp. 9–17, 2007.
- [4] S. N. Napoleon and M. Sampei, “Balance control analysis of humanoid robot based on ZMP feedback control,” in *Proc. IEEE/RSJ Int. Conf. Intell. Robots Syst.*, 2002, vol. 3, pp. 2437–2442.
- [5] A. Goswami, “Postural stability of biped robots and the foot-rotation indicator (FRI) point,” *Int. J. Robot. Res.*, vol. 18, no. 6, pp. 523–533, 1999.
- [6] C. Chevallereau, E. R. Westervelt, and J. W. Grizzle, “Asymptotically stable running for a five-link, four-actuator, planar bipedal robot,” *Int. J. Robot. Res.*, vol. 24, no. 6, pp. 431–464, 2005.
- [7] E. R. Westervelt, J. W. Grizzle, and D. E. Koditschek, “Hybrid zero dynamics of planar biped walkers,” *IEEE Trans. Autom. Control*, vol. 48, no. 1, pp. 42–56, Jan. 2003.
- [8] M. Nikkha, H. Ashrafiuon, and F. Fahimi, “Robust control of underactuated bipeds using sliding modes,” *Robotica*, vol. 25, no. 3, pp. 367–374, May 2007.
- [9] M. D. Berkemeier and R. S. Fearing, “Tracking fast inverted trajectories of the underactuated acrobot,” *IEEE Trans. Robot. Autom.*, vol. 15, no. 4, pp. 740–750, Aug. 1999.
- [10] A. Isidori, *Nonlinear Control Systems*. New York: Springer-Verlag, 1995.
- [11] D. E. Koditschek and M. Buhler, “Analysis of a simplified hopping robot,” *Int. J. Robot. Res.*, vol. 10, no. 6, pp. 587–605, 1991.
- [12] M. H. Raibert, H. B. Brown, Jr., and M. Chepponis, “Experiments in balance with a 3D one-legged hopping-machine,” *Int. J. Robot. Res.*, vol. 3, no. 2, pp. 75–92, 1984.
- [13] S. Kajita, T. Nagasaki, K. Kaneko, K. Yokoi, and K. Tanie, “A hop towards running humanoid biped,” in *Proc. IEEE Int. Conf. Robot. Autom.*, 2004, vol. 1, pp. 629–635.
- [14] Honda Private Ltd. (2009, Mar. 30). [Online]. Available: <http://world.honda.com/HDTV/ASIMO/>
- [15] K. Arikawa and T. Mita, “Desing of multi-DOF jumping robot,” in *Proc. IEEE Int. Conf. Robot. Autom.*, 2002, pp. 3992–3997.
- [16] S. Sakka and K. Yokoi, “Humanoid vertical jumping based on force feedback and inertial forces optimization,” in *Proc. IEEE Int. Conf. Robot. Autom.*, Apr. 18–22, 2005, pp. 3752–3757.
- [17] V. Nunez and N. Nadjar-Gauthier, “Control strategy for vertical jump of humanoid robots,” in *Proc. IEEE/RSJ Int. Conf. Intell. Robots Syst.*, Aug. 2–6, 2005, pp. 2253–2258.
- [18] T. Hirano, T. Sueyoshi, and A. Kawamura, “Development of ROCOS (robot control simulator)-jump of human-type biped robot by the adaptive impedance control,” in *Proc. 6th Int. Workshop Adv. Motion Control*, Apr. 2000, pp. 606–611.
- [19] N. Shiraiishi, Y. Kawaida, Y. Kitamura, S. Nakaura, and M. Sampei, “Vertical jumping control of an Acrobat Robot with consideration of input timing,” in *Proc. 41st SICE Annu. Conf.*, Aug. 5–7, 2002, vol. 4, pp. 2531–2536.
- [20] T. Mita, S. H. Hyon, and T. K. Nam, “Analytical time optimal control solution for a two-link planar aerobot with initial angular momentum,” *IEEE Trans. Robot. Autom.*, vol. 17, no. 3, pp. 361–366, Jun. 2001.
- [21] M. Sobotka and M. Buss, “Locomotion studies for a 5DoF gymnastic robot,” in *Proc. IEEE/RSJ Int. Conf. Intell. Robots Syst.*, Aug. 2005, pp. 3275–3280.
- [22] K. Mirza, M. D. Hanes, and D. E. Orin, “Dynamic simulation of enveloping power grasps,” in *Proc. IEEE Int. Conf. Robot. Autom.*, May 2–6, 1993, vol. 2, pp. 430–435.
- [23] S. H. Hyon, N. Yokoyama, and T. Emura, “Back handspring of a multi-link gymnastic robot—Reference model approach,” *Adv. Robot.*, vol. 20, no. 1, pp. 93–113, 2006.
- [24] M. Yamakita, M. Kishikawa, and T. Sadahiro, “Motion control for robust landing of acrobat robot,” in *Proc. IEEE/RSJ Int. Conf. Intell. Robots Syst.*, 2003, pp. 1141–1146.
- [25] Y. Hurmuzlu and D. B. Marghitu, “Rigid body collisions of planar kinematic chains with multiple contact points,” *Int. J. Robot. Res.*, vol. 13, no. 1, pp. 82–92, 1994.

- [26] M. W. Spong and M. Vidyasagar, *Robot Dynamic and Control*. New York: Wiley, 1989.
- [27] J. J. Craig, *Introduction to Robotics: Mechanics and Control*, 2nd ed. Boston, MA: Addison-Wesley/Longman, 1989.
- [28] H. K. Khalil, *Nonlinear Systems*, 2nd ed. Englewood Cliffs, NJ: Prentice-Hall, 1996.
- [29] T. F. Coleman and Y. Li, "An interior trust region approach for nonlinear minimization subject to bounds," *SIAM J. Optim.*, vol. 6, pp. 418–445, 1996.
- [30] A. Meghdari and M. Aryanpour, "Dynamic modeling and analysis of the human jumping process," *J. Intell. Robot. Syst.*, vol. 37, pp. 97–115, 2003.
- [31] M. S. Branicky, "Multiple Lyapunov functions and other analysis tools for switched and hybrid systems," *IEEE Trans. Autom. Control*, vol. 43, no. 4, pp. 475–482, Apr. 1998.
- [32] B. Morris and J. W. Grizzle, "A restricted Poincaré map for determining exponentially stable periodic orbits in systems with impulse effects: Application to bipedal robots," in *Proc. 44th IEEE Conf. Decis. Control, Eur. Control Conf.*, Dec. 2005, pp. 4199–4206.
- [33] K. W. Sok, M. Kim, and J. Lee, "Simulating biped behaviors from human motion data," *ACM Trans. Graph.*, vol. 26, no. 3, article 107, 2007.
- [34] E. R. Westervelt, J. W. Grizzle, C. Chevallereau, J. Choi, and B. Morris, *Feedback Control of Dynamic Bipedal Robot Locomotion*. Boca Raton, FL: CRC, 2007.



Dip Goswami (S'08) received the B.E. degree in electrical engineering from Jadavpur University, Kolkata, India, in 2000, the M.Tech degree from the Indian Institute of Technology Kanpur, Kanpur, India, in 2005, and the Ph.D. degree from the Department Electrical and Computer Engineering, National University of Singapore (NUS).

He is currently a Research Fellow with the Department of Computer Science, NUS. His current research interests include humanoid robotics, underactuated biped robots, nonlinear dynamics, and control.



Prahlad Vadakkepat (M'00–SM'05) received the M.Tech and Ph.D. degrees from the Indian Institute of Technology Madras, Chennai, India, in 1989 and 1996, respectively.

From 1991 to 1996, he was a Lecturer with the Regional Engineering College Calicut (now the National Institute of Technology Calicut), Kerala, India. From 1996 to 1998, he was with the Korea Advanced Institute of Science and Technology, Daejeon, Korea, as a Postdoctoral Fellow. He is currently an Associate Professor with the National University of Singapore.

Since 2003, he has been an Associate Editor of the *International Journal of Humanoid Robotics*. His current research interests include humanoid robotics, distributed robotic systems, evolutionary robotics, neuro-fuzzy controllers, and intelligent control techniques.

Dr. Vadakkepat is the Founder Secretary of the Federation of International Robot-Soccer Association, where he is currently the General Secretary. From 2001 to 2002, he was appointed as the Technical Activity Coordinator of IEEE Region 10.